



# EDGEWOOD

## CHEMICAL BIOLOGICAL CENTER

U.S. ARMY RESEARCH, DEVELOPMENT AND ENGINEERING COMMAND

ECBC-TR-607

**CALCULATIONS OF LIGHT SCATTERING MEASUREMENTS  
PREDICTING SENSITIVITY  
OF DEPOLARIZATION TO SHAPE CHANGES  
OF SPORES AND BACTERIA**

Stephen D. Druger

UNIVERSITY OF MASSACHUSETTS-LOWELL  
Lowell, MA 01854



Jozsef Czege  
Zhao Z. Li

UNIFORMED SERVICES UNIVERSITY  
OF THE HEALTH SCIENCES  
Bethesda, MD 20814



UNIFORMED SERVICES UNIVERSITY  
*of the Health Sciences*

Burt V. Bronk

AIR FORCE RESEARCH LABORATORY  
Wright-Patterson AFB, OH 45433



April 2008

Approved for public release;  
distribution is unlimited.



# 20080605089

ABERDEEN PROVING GROUND, MD 21010-5424

#### Disclaimer

The findings in this report are not to be construed as an official Department of the Army position unless so designated by other authorizing documents.

REPORT DOCUMENTATION PAGE				Form Approved OMB No. 0704-0188	
Public reporting burden for this collection of information is estimated to average 1 hour per response, including the time for reviewing instructions, searching existing data sources, gathering and maintaining the data needed, and completing and reviewing this collection of information. Send comments regarding this burden estimate or any other aspect of this collection of information, including suggestions for reducing this burden to Department of Defense, Washington Headquarters Services, Directorate for Information Operations and Reports (0704-0188), 1215 Jefferson Davis Highway, Suite 1204, Arlington, VA 22202-4302. Respondents should be aware that notwithstanding any other provision of law, no person shall be subject to any penalty for failing to comply with a collection of information if it does not display a currently valid OMB control number. PLEASE DO NOT RETURN YOUR FORM TO THE ABOVE ADDRESS.					
1. REPORT DATE (DD-MM-YYYY) XX-04-2008		2. REPORT TYPE Final		3. DATES COVERED (From - To) Mar 2005 - Nov 2007	
4. TITLE AND SUBTITLE Calculations of Light Scattering Measurements Predicting Sensitivity of Depolarization to Shape Changes of Spores and Bacteria				5a. CONTRACT NUMBER W91ZLK-05-P-0691	
				5b. GRANT NUMBER	
				5c. PROGRAM ELEMENT NUMBER	
6. AUTHOR(S) Druger, Stephen D. (UMASS); Czege, Jozsef; Li, Zhao Z. (USUHS); and Bronk, Burt V. (AFRL)*				5d. PROJECT NUMBER	
				5e. TASK NUMBER	
				5f. WORK UNIT NUMBER	
7. PERFORMING ORGANIZATION NAME(S) AND ADDRESS(ES) UMASS-Lowell, Lowell, MA 01854 USUHS, Bethesda, MD 20814 AFRL/RHPC, WPAFB, OH 45433				8. PERFORMING ORGANIZATION REPORT NUMBER ECBC-TR-607	
9. SPONSORING / MONITORING AGENCY NAME(S) AND ADDRESS(ES)				10. SPONSOR/MONITOR'S ACRONYM(S)	
				11. SPONSOR/MONITOR'S REPORT NUMBER(S)	
12. DISTRIBUTION / AVAILABILITY STATEMENT Approved for public release; distribution is unlimited.					
13. SUPPLEMENTARY NOTES *At the time this work was conducted, Dr. Bronk was also assigned as Air Force Liaison to U.S. Army Edgewood Chemical Biological Center Aerosol Science Team, APG, MD 21010-5424.					
14. ABSTRACT This report presents calculations to explore the use of depolarization of scattered light as a discriminator of biological particles in an aerosol. The discrete dipole approximation was used to model appropriate shapes of several different types of particles. To model an ensemble of spores, we used experimental parameters appropriate to <i>Bacillus cereus</i> . For this case, two different but related assumptions for particle shapes are shown to give different and distinguishable graphs for the depolarization, <i>D</i> , as a function of wavelength and scattering angle. The use of two different length distributions to simulate scattering from two different strains of <i>Escherichia coli</i> gave rise to distinguishable graphs for <i>D</i> for the two strains. Here, the same shape (hemispherically-capped cylinder) as well as the same value for other parameters (i.e., width and refractive index) was assumed for the two strains. In the preceding calculations, we averaged over random orientations and size distributions based on experimental measurements for a real aerosol. The calculated results predict that <i>D</i> would provide some identification of aerosols made up largely of single biological particles. Calculations were also performed for small clusters made up of several spherical spores.					
15. SUBJECT TERMS Light scattering      Depolarization      Aerosols      Bacteria      Spores      Sensitivity to shape					
16. SECURITY CLASSIFICATION OF:			17. LIMITATION OF ABSTRACT	18. NUMBER OF PAGES	19a. NAME OF RESPONSIBLE PERSON
a. REPORT	b. ABSTRACT	c. THIS PAGE			Sandra J. Johnson
U	U	U	UL	45	19b. TELEPHONE NUMBER (include area code) (410) 436-2914

Blank



## EXECUTIVE SUMMARY

This report presents calculations to explore the use of depolarization of scattered light as a discriminator of biological particles in an aerosol. The discrete dipole approximation was used to model appropriate shapes of several different types of particles.

To model an ensemble of spores, we used experimental parameters appropriate to *Bacillus cereus*. For this case, two different but related assumptions for particle shapes are shown to give different and distinguishable graphs for the depolarization  $D(\Theta, \lambda)$  as a function of wavelength and scattering angle.

The use of two different length distributions to simulate scattering from two different strains of *Escherichia coli* gave rise to distinguishable graphs for  $D(\Theta, \lambda)$  for the two strains. Here, the same shape (hemispherically-capped cylinder) as well as the same value for other parameters (i.e., width and index of refraction) was assumed for the two strains.

In the preceding calculations, we averaged over random orientations and size distributions based on experimental measurements for a real aerosol. The calculated results predict that  $D(\Theta, \lambda)$  would provide some identification of aerosols made up largely of single biological particles.

The Mueller matrix elements  $S_{11}(\Theta)$  and  $S_{22}(\Theta)$  are identically equal for a spherical scatterer, so that  $D(\Theta, \lambda) = 1 - S_{22} / S_{11}$  is identically zero for an aerosol composed of perfect spheres. Spherical background particles mixed in with the bacteria affect the angular dependence of the depolarization  $D(\Theta, \lambda)$  only by affecting the average  $S_{11}(\Theta)$  and average  $S_{22}(\Theta)$  for the aerosol in the same way, leading to a predictably small effect on  $D(\Theta, \lambda)$  in this idealized model case. The scattering predicted for such a mixture probably would be similar to what would be observed from spores or bacteria in an aerosol with a large portion of liquid microdroplets.

Clusters of particles are also observed in biological aerosols. To keep the calculation tractable for the case of clusters, individual spores making up each cluster were assumed spherical, and calculations of  $D(\Theta, \lambda)$  were made for plausible clusters of six to eight of these "spore spheres." Results are presented for two different geometries of seven spore-sphere clusters indicating the extent to which the tightness of the cluster affects the graph of  $D(\Theta, \lambda)$ .

Blank

## PREFACE

The work described in this report was authorized under Contract No. W91ZLK-05-P-0691. The work was started in March 2005 and completed in November 2007.

The use of either trade or manufacturers' names in this report does not constitute an official endorsement of any commercial products. This report may not be cited for purposes of advertisement.

This report has been approved for public release. Registered users should request additional copies from the Defense Technical Information Center; unregistered users should direct such requests to the National Technical Information Service.

Blank



## CONTENTS

1.	INTRODUCTION .....	11
2.	THEORETICAL CONSIDERATIONS .....	12
2.1	Scattering Matrix Elements.....	13
2.2	Coupled-Dipole Method .....	15
3.	PARAMETERS AND ASSUMPTIONS.....	16
3.1	Bacillus Endospores.....	17
3.2	Vegetative Bacteria.....	19
3.3	Spore Clusters .....	21
3.4	Solution of the DDA Equations .....	23
3.5	Calculations for Spore Clusters .....	23
3.6	Orientation Averaging .....	26
4.	RESULTS FOR INDIVIDUAL PARTICLES .....	28
4.1	Spores .....	28
4.2	Vegetative Bacteria.....	34
4.3	Particles that have Almost Zero Depolarization .....	38
4.4	Clusters of Spores .....	38
4.5	Scattering from Disks .....	43
5.	CONCLUSIONS AND RECOMMENDATIONS .....	43
	LITERATURE CITED .....	45

## FIGURES

1.	Scattering coordinate system .....	13
2.	Length and diameter distribution for <i>Bacillus cereus</i> spores.....	17
3.	Distribution of diameters and lengths used in modeling <i>B. cereus</i> spores .....	18
4.	Length distribution for <i>E. coli</i> B/r.....	20
5.	Length distribution for <i>E. coli</i> K12.....	20
6.	Compact Cluster.....	25
7.	Two views of the Loose Cluster .....	25
8.	Single random orientation vs. average for the Compact 7 spore-sphere cluster.....	27
9.	Comparison of various mesh sizes for the Compact 7 spore-sphere cluster.....	27
10.	Depolarization ratio for capped cylinder of length 1.5 $\mu\text{m}$ and radius 0.35 $\mu\text{m}$ averaged only over orientation, at wavelength 1.551 $\mu\text{m}$ , $n = 1.503 + 0.000402 i$ .....	28
11.	Mueller matrix element $S_{11}$ for an ensemble of spores averaged only over orientations for the single size spore with length 1.25 $\mu\text{m}$ , and diameter or minor axis of 0.72 $\mu\text{m}$ .....	29
12.	Mueller matrix element $S_{22}$ for an ensemble of spores averaged only over orientations for the single size spore with length 1.25 $\mu\text{m}$ , and diameter or minor axis of 0.72 $\mu\text{m}$ . The scattering wavelength is 266 nm .....	29
13.	Depolarization for ensemble of spores of single size with length 1.25 $\mu\text{m}$ and diameter 0.72 $\mu\text{m}$ averaged only over orientation, with no size average....	30
14.	Depolarization ratio comparison for two spore models averaged over size and orientation at 266-, 410-, and 1551-nm wavelengths.....	30
15.	Depolarization ratio comparison for two spore models averaged over size and orientation at 355- and 750-nm wavelengths.....	31
16.	Depolarization ratio comparison for two spore models averaged over size and orientation at 460-nm wavelength .....	32

17.	Graphs for the depolarization at IR wavelengths for averaging as in Figure 14.....	32
18.	Backscattering ( $\Theta = 180^\circ$ ) depolarization for two particle shape models of single spores, both models averaged for size and orientation with <i>B. cereus</i> spore parameters .....	33
19.	Mueller matrix elements $S_{11}$ and $S_{22}$ vs. angle at wavelength 355 nm for rod-shaped bacteria with <i>Escherichia coli</i> B/r-like parameters, averaged over length and orientation .....	34
20.	Mueller matrix elements $S_{11}$ and $S_{22}$ vs. angle at wavelength 355 nm for rod-shaped bacteria with K12-like parameters.....	35
21.	Depolarization vs. angle at wavelength 355 nm for rod-shaped bacteria with B/r-like parameters (shorter lengths) .....	35
22.	Depolarization vs. angle at wavelength 355 nm for rod-shaped bacteria with K12-like parameters (longer lengths) .....	36
23.	Depolarization vs. angle at longer wavelengths for rod-shaped vegetative bacteria.....	37
24.	Graphs of depolarization vs. angle with averaging over orientation along with averaging over every width together with every length for distributions defined in Section 3.1 .....	38
25.	Calculation using seven spore-spheres each with approximately 400 dipoles compared with calculation using only seven dipoles .....	39
26.	Depolarization vs. scattering angle for the Loose and the Compact spore-sphere clusters of seven spores for scattering wavelength $1.551\ \mu\text{m}$ .....	40
27.	Depolarization vs. scattering angle for wavelength $1.551\ \mu\text{m}$ for the Compact Cluster.....	41
28.	Depolarization vs. angle for Loose and Compact Clusters for scattering at wavelength $3.389\ \mu\text{m}$ , refractive index of spore spheres is $1.511 + 0.0136\ i$ .....	42
29.	Depolarization vs. angle for scattering at wavelength $3.389\ \mu\text{m}$ from the Compact Cluster of spores .....	42
30.	Depolarization vs. angle for scattering from randomly oriented disks using a $27 \times 51$ grid in $(\theta, \phi)$ for the sizes shown.....	43

## TABLES

1.	Refractive Index of <i>B. cereus</i> Spores at Representative Wavelengths .....	18
2.	Length Distribution for <i>E. coli</i> B/r.....	20
3.	Diameter Distribution for <i>E. coli</i> B/r .....	20
4.	Length Distribution for <i>E. coli</i> K12.....	20
5.	Coordinates of Spore-Sphere Centers for Compact Cluster .....	25
6.	Coordinates for Loose Cluster .....	26



# CALCULATIONS OF LIGHT SCATTERING MEASUREMENTS PREDICTING SENSITIVITY OF DEPOLARIZATION TO SHAPE CHANGES OF SPORES AND BACTERIA

## 1. INTRODUCTION

There has been practical interest in determining whether polarized light scattering would provide important input into determining the nature of an aerosol containing biological particles. This is of interest both for lidar backscatter and for point measurements where samples of the aerosol are drawn through an instrument.

Bacterial scatterers of light in an aerosol differ in size, refractive index, or shape from the background particles that may be present. Many of the background scatterers, for example, are flat. Other scatterers are irregular in shape but are often modeled in calculations as spheres. Various particles may also clump together to form clusters. However, bacterial particles are ellipsoidal, or have the shape of a prolate spheroid, or often have a shape well approximated by capped cylinders. Depolarization in scattering may help classify aerosol particles according to their shape. For example, scattering from perfect spheres produces no depolarization, while scattering from ellipsoids and many other non-spherical shapes can produce considerable depolarization. Thus, the polarization of the backscattering has particular interest as a potential probe.

Recent experimental work examined the polarization of backscatter signals for aerosolized BG (*Bacillus atrophaeus*) spores mixed with naturally occurring organic and inorganic background aerosol materials.<sup>1</sup> Certain polarization ratios of the backscattered light appeared to be potentially useful as discriminants. A particularly interesting variation in the energy normalized depolarization ratio at 1551 nm divided by the depolarization ratio at 3389 nm was observed and might be useful in identifying aerosols containing bacterial endospores. Moreover, it was proposed that the large imaginary part of the refractive index around 3389 nm might suppress depolarization by the bacterial component near that wavelength.<sup>1</sup>

In the present work, we examine similar questions using a theoretical-computational approach based on modeling the scattering of aerosols containing microorganisms, including mixtures of microorganisms and background particles. Such an approach based on computational modeling offers the advantage of allowing us to study the variation of the scattering with parameters in ways that may not be feasible experimentally (e.g., by computationally or analytically varying the ratios of the different particulates once the scattering patterns for each has been determined).

Our basic approach is to compute the set of Mueller matrix elements  $\{S_{ij}^I\}$  for scattering angles between  $0^\circ$  and  $180^\circ$ , for each model particle type  $I$  of interest, averaging over orientations and where appropriate over size distributions. Then, with  $\beta_I$  denoting the fraction of particles of type  $I$ , the appropriately averaged Mueller matrix element,  $S_{ij}$ , can be obtained as

$$\langle S_{ij} \rangle = \sum_I \beta_I S_{ij}^I \quad (1)$$

where  $S_{ij}^I$  for each species includes an average over particle orientations.

The methods we use for the non-spherical particles are an extension of those in previous studies by the present authors and co-workers who applied the discrete dipole approximation (DDA), also known as the "coupled-dipole model," to calculate scattering matrix elements for light scattering from randomly oriented targets.<sup>2,3,4</sup> For the simple case of spherical background scatterers in some of our model calculations, we use the Mie scattering program of Bohren and Huffman.<sup>5</sup>

Our previous studies used the DDA to examine light scattering patterns from randomly oriented *Escherichia coli* bacteria *in vivo* by modeling them as capped cylinders with a distribution of lengths and diameters. Detailed comparison with experimental data gave good agreement and supported the conclusion that observation of the ratio of light scattering (Mueller) matrix elements  $\langle S_{34} \rangle / \langle S_{11} \rangle$  provides a rapid and convenient method of monitoring bacterial diameters *in vivo* even when there is an appreciable distribution of lengths in the bacterial population. In many respects, the present modeling is an extension of this previous work; in particular, our model calculations of the depolarization from *E. coli* based on experimental size distributions in Section 4.2 builds upon the earlier work.

The biological material we considered in the present work included spheroidal spore shapes, bacteria (e.g., *E. coli*, whose shape can be approximated as that of a capped cylinder), and spore clusters. Because realistic background particles occur in various sizes, we performed model simulations with experimentally observed size distributions and random orientations of bacteria and idealized background particles.

In Section 2, we present some of the relevant theoretical background.

## 2. THEORETICAL CONSIDERATIONS

We assume light incident along the  $z$  axis with the coordinate system defined in accordance with the conventions given in Bohren and Huffman<sup>5</sup> and illustrated in Figure 1. The scattering plane is the plane containing the  $z$  axis and the scattering direction vector labeled  $\mathbf{k}$ .

The polarization state of either the incident or scattered light is described by the Stokes parameters  $I$ ,  $Q$ ,  $U$ , and  $V$ . The first parameter  $I$  is the total irradiance that would be observed without a polarizer. The second parameter  $Q$  is the difference in irradiances polarized parallel to the scattering plane and perpendicular to the scattering plane, and would be measured using parallel and perpendicular polarizers. The third parameter  $U$  is obtained by rotating a parallel polarizer by  $+45^\circ$  and  $-45^\circ$  and calculating the difference in measured irradiances. The fourth parameter  $V$  is the difference in right and left circularly polarized irradiances.



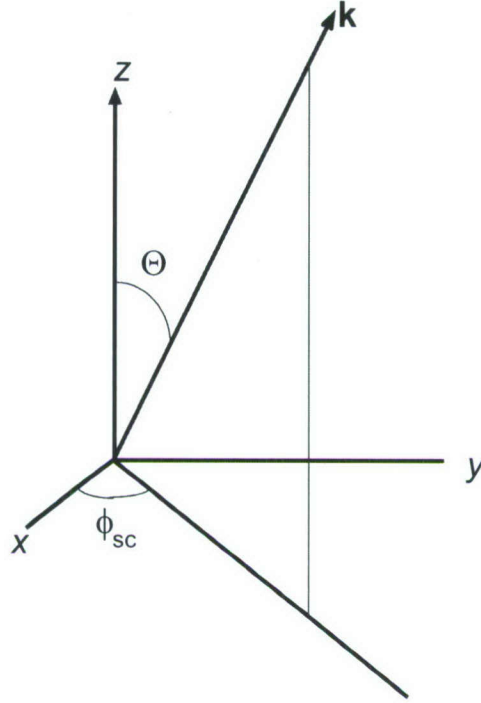


Figure 1. Scattering coordinate system. The light is incident along the z direction, and the scattering is calculated in the direction  $\mathbf{k}$ , with scattering angle  $\Theta$

## 2.1 Scattering Matrix Elements

A calculation of the scattered fields for scattering in a particular direction of incident light, in particular polarization states, leads to a linear relation between the Stokes parameters of the incident and scattered light. The specification of the coefficients in this relation describes the scattering. For example, the relation between field polarizations amplitudes  $E_{\parallel}$  parallel to the scattering plane and  $E_{\perp}$  perpendicular to the scattering plane for input and scattered light are given by the amplitude scattering matrix

$$\begin{pmatrix} E_{\parallel s} \\ E_{\perp s} \end{pmatrix} = \frac{e^{ik(r-z)}}{-ikr} \begin{pmatrix} S_2 & S_3 \\ S_4 & S_1 \end{pmatrix} \begin{pmatrix} E_{\parallel i} \\ E_{\perp i} \end{pmatrix}. \quad (2)$$

The electric field vector on the right hand side of eq. 2 refers to the incoming light, and that on the left is the field for the scattered light.

Each of the elements of the amplitude matrix is complex valued. The phase of the matrix elements almost never can be determined relative to other particles in an ensemble. Therefore, we confine our attention to calculations that do not depend on the relative phases (e.g., by disregarding multiple scattering). Single particle scattering dominates measurements in all observations of aerosols where the particle density is small, as is the usual case.

The  $4 \times 4$  Mueller matrix for a single scatterer contains all the polarization and amplitude information of the light scattered from either a single particle or an ensemble of particles that receive the same input light. The elements of that matrix may be derived from the elements of the amplitude matrix for a single particle. The simple equations relating the elements of these matrices are given in Reference 5. All elements of the Mueller matrix are real, and are additive for all the scattering particles. Thus, we may calculate the Mueller matrix for each particle in an ensemble and then average over all of these matrices to get the Mueller matrix for the ensemble.

The Mueller matrix elements  $\{S_{ij}\}$  describing the scattering in a particular scattering direction  $(\Theta, \phi_{sc})$  are then the 16 elements of the matrix relating the Stokes parameters for the incoming light and the scattered light in the scattering direction

$$\begin{pmatrix} I_s \\ Q_s \\ U_s \\ V_s \end{pmatrix} = \frac{e^{ik(r-z)}}{-ikr} \begin{pmatrix} S_{11} & S_{12} & S_{13} & S_{14} \\ S_{21} & S_{22} & S_{23} & S_{24} \\ S_{31} & S_{32} & S_{33} & S_{34} \\ S_{41} & S_{42} & S_{43} & S_{44} \end{pmatrix} \begin{pmatrix} I_i \\ Q_i \\ U_i \\ V_i \end{pmatrix}. \quad (3)$$

If the values of the fields in eq. 2 are evaluated computationally for each scattering angle of interest, then eq. 2 allows the four scattering amplitudes  $S_j$  to be calculated at each scattering angle, and the Mueller matrix elements follow from the four  $S_j$  amplitudes. For example,  $S_{11}$  measures the total scattering for unpolarized incident light

$$S_{11} = \frac{1}{2} (|S_1|^2 + |S_2|^2 + |S_3|^2 + |S_4|^2), \quad (4)$$

while the value of  $S_{22}$  depends on changes in polarization

$$S_{22} = \frac{1}{2} (|S_1|^2 + |S_2|^2 - |S_3|^2 - |S_4|^2). \quad (5)$$

In particular, the depolarization ratio  $D$ , defined as

$$D = 1 - \frac{S_{22}}{S_{11}}, \quad (6)$$

is of special interest in the present work. Note that  $S_{22}$  differs from  $S_{11}$  only because of the presence of nonzero values of  $|S_3|^2 + |S_4|^2$  according to eqs. 3-5. But,  $S_3$  and  $S_4$  are seen in eq. 2 to describe the change from polarization in one direction to the polarization in the cross direction to it. For perfectly spherical scatterers,  $S_3 = S_4 = 0$ , which gives no change in polarization direction. This means that  $S_{22} = S_{11}$  for such scatterers. Hence, the depolarization ratio  $D(\Theta, \lambda)$  is identically equal to zero at all scattering angles  $\Theta$  when the scatterers have an exact spherical symmetry.



The Mueller matrix elements are computed by calculating the scattered fields for the various polarization of incident field in eq. 3. This determines the scattering amplitudes, and therefore the Mueller matrix elements of interest. For the case of spherical scatterers, the present work uses the Mie solution to calculate the scattered fields and Mueller matrix elements for each scattering angle. For other particle shapes, we use variants of the coupled-dipole method first introduced by Purcell and Pennypacker,<sup>2</sup> and also known as the DDA method.

The DDA method is based on replacing the scatterer by a finite array of polarizable sites, which can be conveniently placed on a cubic lattice within the volume of the scatterer. The polarizable sites are subject to an incident oscillating electromagnetic field. Let  $\mathbf{E}_0$  be the vector amplitude of the incident electric field  $\mathbf{E}(\mathbf{r}, t) = \mathbf{E}_0 \exp[i(\mathbf{k} \cdot \mathbf{r} - \omega t)]$  where  $\mathbf{k}$  is the wave vector, and the location of dipole  $i$  is at position  $\mathbf{r}_i$ . The electric field that the dipole  $\boldsymbol{\mu}_j$  at position  $\mathbf{r}_j$  produces at site  $i$  located at position  $\mathbf{r}_i$  is

$$\mathbf{E}(\mathbf{r}_i) = \mathbf{T}_{ij} \cdot \boldsymbol{\mu}_j \quad (7)$$

where

$$\boldsymbol{\mu}_j = \alpha \mathbf{E}(\mathbf{r}_j) \quad (8)$$

and where  $\alpha$  is the polarizability for the dipoles. The resulting field at  $\mathbf{r}_i$  from all the other dipoles and from the applied (complex) field  $\mathbf{E}_0(\mathbf{r}_i)$  is

$$\mathbf{E}(\mathbf{r}_i) = \mathbf{E}_0(\mathbf{r}_i) + \sum_j \mathbf{T}_{ij} \cdot \alpha \mathbf{E}(\mathbf{r}_j). \quad (9)$$

In terms of the components involved,

$$E(i\xi) = E_0(i\xi) + \sum_{j=1}^N \sum_{\nu=1}^3 \alpha T(i\xi; j\nu) \cdot E(j\nu), \quad (10)$$

where  $\mathbf{T}$  denotes the complex dipole-dipole coupling matrix for the  $N$  dipoles, for wavelength  $\lambda$ , and refractive index  $n$  of the particles. Note that  $\mathbf{T}$  depends on wavelength, and on the relative locations of the dipole sites, but does not depend on the refractive index  $n$  or on the polarizability  $\alpha$  derived from  $n$  via the Clausius-Mossotti relation. Specifically,<sup>2</sup>

$$T(i\xi; j\nu) = \frac{\exp(ikr_{ij})}{r_{ij}^3} \left[ k^2 r_{ij}^2 \left( \frac{ikr_{ij} - 1}{r_{ij}^2} + k^2 r_{ij}^2 \right) \delta_{\xi\nu} + \left( \frac{3(ikr_{ij} - 1)}{r_{ij}^2} - k^2 \right) (\mathbf{r}_{ij})_{\xi} (\mathbf{r}_{ij})_{\nu} \right]. \quad (11)$$

A matrix element of  $\mathbf{T}$  is labeled here as  $\mathbf{T}(i\xi; j\nu)$  corresponding to interaction between the dipole  $i$  and the dipole  $j$  (for  $\xi = 1, 2, 3$  labeling, respectively, the  $x$ ,  $y$ , and  $z$  coordinates, and

similarly for  $\nu = 1, 2, 3$ ). Also  $(\mathbf{r}_{ij})_\xi$  denotes the  $\xi$  component of the displacement vector of site  $i$  relative to site  $j$ . Equation (10) can be rewritten as

$$\sum_{j=1}^N \sum_{\nu=1}^3 [\delta_{ij} \delta_{\xi\nu} - \alpha T(i\xi; j\nu)] E(j\nu) = E_0(i\xi) \quad (12)$$

which is the equation that is solved to find the field and the dipole moment at each site. It can be expressed in matrix form as

$$[\mathbf{1} - \alpha \mathbf{T}] \bullet \mathbf{E} = \mathbf{E}_0 \quad (13)$$

with  $\mathbf{1}$  denoting the unit matrix.

We assume  $\alpha$  to be determined by the refractive index  $n$  of the continuous dielectric particle being represented through the Clausius-Mossotti relation

$$\alpha = \frac{3}{M\pi} \frac{n^2 - 1}{n^2 + 2} \quad (14)$$

where  $M$  is the number of dipole sites per unit volume.

Although various refinements and improvements of the DDA method have been proposed, the basic DDA procedure just described has led to reasonably accurate calculation of Mueller matrix elements using surprisingly small numbers of dipoles to represent the scatterer, and has proven useful for modeling scattering from bacterial systems.<sup>3</sup>

### 3. PARAMETERS AND ASSUMPTIONS

In this section, we describe some model biological particles used in this report, and present the rationale for the optical parameters and distributions we use. The models and the parameters were chosen as examples to explore and illustrate the possible importance of depolarization measurements as a means to optically characterize some representative bioparticles and backgrounds, and are not meant to be exhaustive. In this project, we examined the behavior of certain particular Mueller matrix elements, and especially the depolarization ratio,  $D(\Theta, \lambda)$ .

In many biological aerosols, single particles dominate. Therefore, we looked at light scattering from ensembles of spores modeled as single particles, and from some examples of aerosols of single vegetative bacteria. We consider *Bacillus* endospores (hereafter simply called spores). There are other types of spores and other types of bacterial spores, but these are not as important right now for our purposes. The Anthrax and other *Bacillus* spores are more precisely named endospores, but are often just called spores.



For the spores, we used parameters appropriate to *Bacillus cereus*. The size distribution for these spores is excerpted from a large unpublished set of electron microscope measurements due to Z. Z. Li, J. Czege, and B. V. Bronk. These measurements are shown in Figure 2.

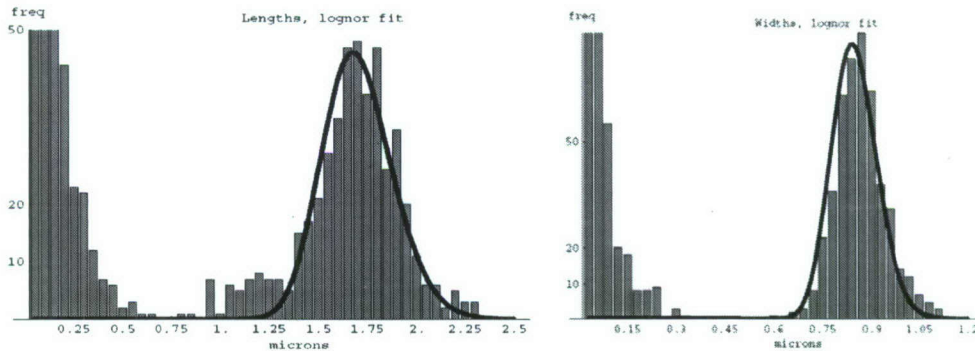


Figure 2. Length (left) and diameter distribution for *Bacillus cereus* spores.

The smoothed distributions under the heavy fitted log-normal graph are representative for these spores. Inspection of the microscope pictures indicated that the small material not associated with the fitted curve was from broken spores or other debris. The diameters (which are the widths in Figure 1) and the lengths were approximately correlated (i.e., longer spores generally have larger diameter). In obtaining the graphs of Figure 2, a small positive correlation was found between lengths and diameters of the spores. To simplify our calculations and reduce computation time, we assumed the correlation was exact (i.e., with a correlation coefficient of 1.0). With this simplifying assumption, we derived five bar histograms from the fitted graphs to be used when size averaging the Mueller matrix elements over single spores. These histograms are shown in Figure 3. In our averaging over sizes, the leftmost diameter is used with the leftmost length and so on.

In addition, we needed real and imaginary parts of the spore index of refraction to allow us to do calculations that should provide results typical for *B. cereus* or other anthrax-like spores. For this, we used interpolated values from the unpublished experimental data of M. Querry (written communication from M. Milham). These values are given in Table 1.

In this study, we use the above parameters for *B. cereus* spores to see what differences in  $D(\Theta, \lambda)$  occur for two different plausible shapes of an individual spore.

In electron microscope pictures of these spores, the individual spores appear like cylinders with rounded ends. Therefore, in our first set of calculations, we used right circular cylinders with radius  $a$ . The model cylinders have hemispherical end-caps of the same radius  $a$  where  $2a$  corresponds to the diameters in Figure 3. If the length of the cylindrical part is  $\ell$ , the overall length is then  $L = \ell + 2a$  where this quantity assumes the value indicated in Figure 3 for the lengths.

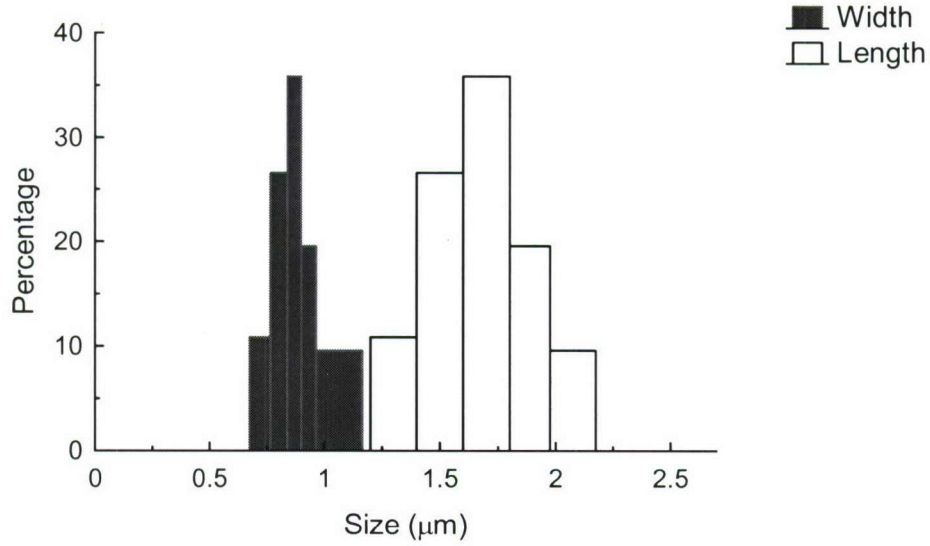


Figure 3. Distribution of diameters (left, black) and lengths used in modeling *B. cereus* spores. The simplifying assumption of direct correlation of length and width (smallest length with smallest width, etc.) is used in the model.

Table 1. Refractive Index of *B. cereus* Spores at Representative Wavelengths

Wavelength (nm)	Real (n)	Im (n)
266	1.619	0.0599
355	1.570	0.000969
410	1.54872	0.000524
1551	1.503	0.0004
3389	1.511	0.0133

In a second set of calculations, we modeled the spores using the shape of a prolate spheroid. For the prolate spheroid, the defining equation is given by

$$(x/a)^2 + (y/a)^2 + (z/b)^2 = 1; \quad \text{where } a < b \quad (15)$$

and  $b$  is the semi-major axis. Then  $2b$  is the length corresponding to  $L$  for the capped cylinders, while  $a$  is the semi-minor axis and the radius of the hemispherical end-cap; hence,  $2a$  was set equal to the values of the diameters in Figure 3.



In each of these two cases, we used the DDA, with single dipole locations filling the space inside the outer boundary defined by the appropriate equation. Roughly 3000 dipoles per spore were used with their location generated as described in Reference 2.

### 3.2 Vegetative Bacteria

Vegetative bacteria come in many forms. However, herein, we consider just one of the important shapes. That is rod-shaped with end-caps similar to hemispheres. In earlier work, we used microscopically measured diameters and lengths as inputs for Mueller matrix calculations based on the DDA model and the capped-cylinder shape. The graph we obtained for  $S_{34} / S_{11}$  gave a good fit to the corresponding graph obtained experimentally.<sup>3</sup>

For the present calculations, we used parameters suggested by those measured for two different strains of *Escherichia coli*. These and other vegetative bacteria have decidedly different refractive indices from Bacillus spores. A refractive index  $n = 1.373 + 0.000396i$  was measured previously<sup>3</sup> and is a good approximate value through the range we model (355 nm or 400 nm wavelength of scattering light) although a slightly larger imaginary part (0.00097) was used in these calculations for vegetative bacteria.

In our first set of calculations relating to these cells, we averaged over orientation as well as the previously measured length distributions for log-phase cells of the bacterial strains B/r and K12 of *Escherichia coli*, but arbitrarily used only a single diameter. The five bar histograms shown in Figures 4 and 5 represent the log-phase lengths measured previously<sup>3,4</sup> for the two different strains. We used these log phase distributions as a model for what might be encountered in an aerosol, and we used the distribution to average over sizes in our calculations. The diameters also have a distribution; however, they were uncorrelated with length, probably because these rod-shaped cells grow by elongation. The K12 bacteria were found to be wider than the B/r bacteria (averaging about 1.05  $\mu\text{m}$  for K12 vs.  $\sim 0.85 \mu\text{m}$  for B/r). However, in the present calculations, we were trying to see how changing just length would affect the depolarization. Therefore, we used the same diameter of 0.85  $\mu\text{m}$  to model both cases. For convenience, we kept this value constant for the initial calculations, rather than averaging over a diameter distribution. Thus, although we label the graphs B/r or K12, we are primarily determining how a substantial change in average length affects  $D(\Theta, \lambda)$  for cells that are otherwise identical.

After the calculations for a single width, we compare the results with those obtained over a distribution of widths and lengths that are assumed uncorrelated with each other. We used a width distribution similar in shape, but narrower than the experimental distribution given in the left hand column of Table 3. For both *E. coli* B/r and the K12 variant, we used the same width distribution as given in the middle column of Table 3. For *E. coli* B/r, we used the length distribution summarized in Table 2, while for K12, we used the length distribution given in Table 4.

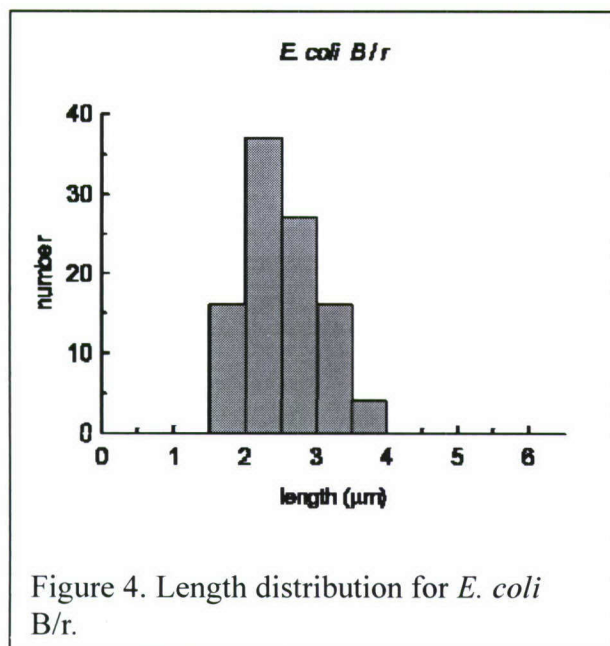


Table 2. Length Distribution for *E. coli B/r*.

Length (μm)	Percent
1.75	16
2.25	37
2.75	27
3.25	16
3.75	4
Total	100

Table 3. Diameter Distribution. *E. coli B/r*.

Experimental Diameters (μm)	Diameters Used in Calculation when Averaging	Percent
0.85	0.7	14
0.9	0.75	36
0.95	0.8	36
1.00	0.85	14

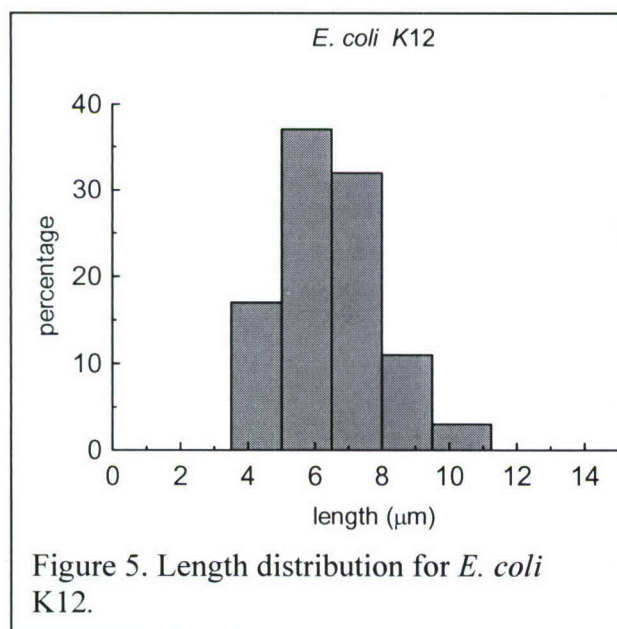


Table 4. Length Distribution for *E. coli K12*.

Length (μm)	Percent
4.25	17
5.75	37
7.25	32
8.75	11
10.25	3
Total	100

The calculations were performed by the same procedures as those used for *B. cereus* using only the hemispherically capped cylinder model. For each calculation, we averaged over the length distributions, and also averaged over orientation using a  $9 \times 15$  mesh in  $\theta$  and  $\phi$ , respectively.



We did some calculations using the somewhat artificial distribution of diameters in the middle column of Table 3 so that we could get good convergence to solutions when doing a full averaging over all lengths (Table 2) with all diameters in the proportions indicated (i.e., without correlation between length and width). We call this “*E. coli* B/r Distribution (A).” For good convergence, the ratio of distance between dipole neighbors to wavelength should be small.<sup>6,7</sup> We compared the resulting graphs for  $D(\Theta, \lambda)$  with the graphs for “*E. coli* B/r Distribution (2/3 A).” For the latter case, the same diameter distribution was used with a length distribution in which each contribution to the average had the same weighting as that given in Table 2. However, each length was shortened to 2/3 the corresponding value in that table.

### 3.3 Spore Clusters

A real aerosol of spores will contain some clusters of spores as well as single spore particles. We modeled a small cluster of approximately 5 to 8 spheres representing a cluster of *Bacillus* endospores, which might be found as individual particles in an aerosol. Each individual spore-sphere representing one spore in the cluster has a diameter  $d$  of approximately 1.0 – 1.5  $\mu\text{m}$ , and our calculations presented here are those for  $d = 1.2 \mu\text{m}$ . The spore radius is  $r = d/2$ . The model spore has a complex refractive index corresponding to the wavelength dependent values given in Table 1.

In an extremely simplified case, the spore-sphere could be represented by a single dipole, which corresponds to the first term in an accurate multipole expansion for a sphere. To examine the extent to which such a simplified model could represent the spores in a cluster, we compared the calculated value of the Mueller matrix ratio  $S_{34}/S_{11}$  for that model with that from a cluster of spore spheres, each represented by numerous dipoles.

#### Approach 1: Simplified DDA model of small cluster of spores.

First, choose as parameters the spore sphere radius  $r$  and the number  $n$  of spore spheres. Each individual spore sphere will be represented by a collection of electric dipoles. We build the model using a simple cubic lattice to locate the spore spheres and also use a finely-spaced simple cubic lattice grid to locate the individual dipoles making up each spore. A super-sphere of radius  $R$  is centered at one of the lattice points, and  $R$  is chosen equal to a representative radius of the actual spore cluster. The spacing of the lattice for positioning the spore sphere is then chosen so that a closely packed set of  $n$  spore spheres each of radius  $r$  will be within radius  $R$  of the origin. The spacing between lattice sites is taken as

$$a = \sqrt[3]{\frac{\frac{4\pi}{3} R^3}{n}} \quad (16)$$

thereby distributing the available space among the spores. However, to avoid overlap of spores, the radius of each spore is then assigned to be half of the lattice spacing, thereby assuring that the spore spheres just barely touch.

A 3-dimensional grid is defined corresponding to a finely-spaced simple cubic lattice. The procedure for constructing this grid is the same as that in our earlier DDA calculation.<sup>2,3,8</sup> The desired number  $N$  of grid points, typically several thousand, to fit into the super-sphere is specified as input. Then the grid lattice spacing is taken as

$$a_{grid} = \sqrt[3]{\frac{4\pi}{3} \frac{R^3}{N}}. \quad (17)$$

This gives approximately, but usually not exactly, the requested number of grid points in the super-sphere. We have shown elsewhere<sup>3</sup> that using several thousand dipoles to represent a single sphere gives results for  $S_{34}/S_{11}$  very closely approximating those computed using the exact Mie expansion.

We use the following procedure for the calculation: Each lattice site that falls within the super-sphere has a spore sphere centered on it. The radius of each spore sphere is half the lattice separation. If the spore spheres are  $\{s_i; i=1, \dots, n\}$ , all points  $< r$  from each of the center points  $s_i$  are inside the  $i^{\text{th}}$  spore sphere with a dipole located on each of them. All other points are in air and are assumed unoccupied by dipoles.

The polarizability of the DDA dipoles is obtained from the Clausius-Mossotti relation, eq. 14, taking the density to be that of the grid lattice.

The scattering is then calculated as a function of angle using the DDA by solving the equation

$$E(i\xi) = E_0(i\xi) + \sum_{j=1}^N \sum_{\nu=1}^3 \alpha T(i\xi; j\nu) E(j\nu) \quad (18)$$

as in our earlier calculations. Here  $E(j\nu)$  is the  $\nu$  component of the induced electric field at dipole site  $j$ ,  $E(i\xi)$  is the  $\xi$  component of the incident electric field at the dipole site  $i$ ,  $\alpha$  is the polarizability, and  $T(i\xi; j\nu)$  is the  $\xi\nu$  component of the dipole-dipole tensor coupling between site  $i$  and site  $j$ . That is, the field component  $E(i\xi)$  produced by dipole components  $\mu(j\nu)$  at each site  $j$  for  $\nu = x, y, z$  is

$$\sum_j \sum_{\nu=1}^3 T(i\xi; j\nu) \mu(j\nu). \quad (19)$$

#### Approach 2: Oversimplified model of small cluster of spores

In the DDA model, the dielectric particle is often thought of as represented by a collection of small polarizable spheres, with only the dipole moment of each sphere to be kept (making it equivalent for light scattering purposes to the corresponding collection of polarizable



point dipoles). If we took the imaginary small spheres in that construction to be the spore spheres, and really kept only the dipole moments in any multipole expansion of the fields, this would involve representing each spore by a single dipole moment.

Moreover, the packing fraction of the spheres would be 0.5. This corresponds closely to the packing fraction measured for spore clusters [unpublished experimental data, Dr. J. Bottiger, U.S. Army Edgewood Chemical Biological Center (ECBC), Aberdeen Proving Ground (APG), MD].

### 3.4 Solution of the DDA Equations

We modified the procedure followed in our earlier work,<sup>2</sup> which involved storing the complete set of dipole-dipole tensors for coupling possible pairs of dipoles. Now, because the grid may have such a large number of sites, most of them unoccupied by dipoles, the dipole-dipole matrix for interactions between all possible sites is too large to store. Therefore, when the program needs to calculate the dipole-dipole matrix contracted with some  $3N$ -dimensional

vector, such as  $\sum_{j=1}^N \sum_{v=1}^3 \alpha T(i\xi; jv) E(jv)$ , it goes through a table of which sites have dipoles on them and sums only over those. It does not store the dipole-dipole interaction between each such pair of sites, but calculates it afresh each time.

The program offers an option of solving the system of equations by simple iteration or by the conjugate gradient method. The simple iteration procedure is usually computationally less costly when it converges, but the conjugate gradient method usually converges when the simple iteration method fails, typically for larger particles, larger refractive index, and smaller wavelength.

### 3.5 Calculations for Spore Clusters

In Section 4.4, we present a calculation that tests the idea of using a single dipole for each sphere compared to using spore spheres in a symmetrical arrangement, and we find that a useful rough approximation can be obtained in that way.

To construct more realistic arrangements of spores into a cluster than placing them on a cubic array, we devised computer algorithms to use the method of Witten and Sander<sup>9</sup> to construct somewhat random arrangements of spores forming the cluster in the previous two cases (dipoles at precise lattice points, and DDA spheres at precise lattice points). We used the following algorithm:

- (1) Place the spheres at random locations, each time checking that the spheres were not assigned to overlap. If any added sphere overlaps other spheres, reject the new location and try again.

- (2) For each sphere

- (a) Displace all the spheres randomly by up to  $\delta$  times its radius vector.

(i) If any sphere then overlaps other spheres, do not accept the new locations, but try again to find a new non-overlapping configuration. (The retry can occur up to 2000 times.)

(ii) For an accepted configuration in (i), if the total displacement squared  $\sum_i |\mathbf{r}_i|^2$  from the origin increases, do not accept the new location but try again at step (i) (up to 500 times)

(iii) For an accepted configuration in (i), if the total displacement squared  $\sum_i |\mathbf{r}_i|^2$  decreases, accept these as the new positions. Then go to step (i) to try again for an even lower total displacement squared.

(iv) If no further reduction in the total displacement squared occurs within 500 consecutive trials, reduce  $\delta$  by multiplying by 0.99 and go to (b) below.

(b) Test if  $\delta$  is large enough ( $>10^{-10}$ ) and restart the search at step (a) if it is. But if  $\delta$  has been reduced to less than  $10^{-10}$  print out the locations of the spheres and exit.

This procedure thereby uses a random walk biased toward particle coalescence to construct the cluster of a few spores (our version of the Witten Sander model).<sup>9,10</sup>

The program for treating the spores as collections of DDA spheres was then modified in two ways. First, we no longer require the spore spheres to be centered each on a grid point. Instead, the output of the program giving the locations of the centers of each spherical spore and its radius (i.e., *position.f*) is read in as input. Secondly, the spores are prevented from overlapping simply by the test within *position.f* that causes it to reject any configurations with overlapping spheres.

The sites on the grid that fall within each assigned spore sphere are taken to have a dipole on each site. Since the spore spheres need not have been taken to be centered on grid points, some may contain more grid points than others, and therefore may contain more dipoles; but, the number will be approximately the same if the sphere radii are considered equal.

We settled on two different clusters of spore spheres as examples for determining what effect differences in the arrangement of the spores would have on the graph of the depolarization. Graphs of the calculations are presented for those clusters in Section 4.4. We call the first of these the “Compact Cluster.” Its shape can be seen in Figure 6. The coordinates of that cluster are given in Table 5.



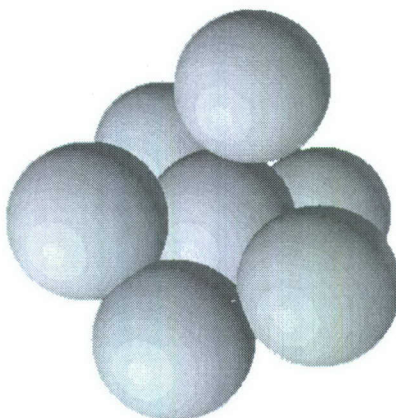


Figure 6. Compact Cluster. Five spheres form a plane with one sphere on top of the center. The lowest sphere in the foreground is slightly below the plane of the five spheres.

Table 5. Coordinates of Spore-Sphere Centers for Compact Cluster

	<b>x</b>	<b>y</b>	<b>z</b>
1	0.10796814E-03	-0.75738501E-01	-0.25377747E-01
2	-1.0337081	0.61300209	-0.33699078E-01
3	1.0404514	-0.77011471	-0.25872477E-01
4	0.19538628	0.66890403	0.95695171
5	-0.42222498	-0.74854324	-1.0420674
6	0.49930960	0.76658113	-0.80320375
7	0.54819461	-0.47870546	1.0590495

Figure 7 shows the other cluster for which calculations are presented, which we refer to as the “Loose Cluster,” for which the coordinates are shown in Table 6.

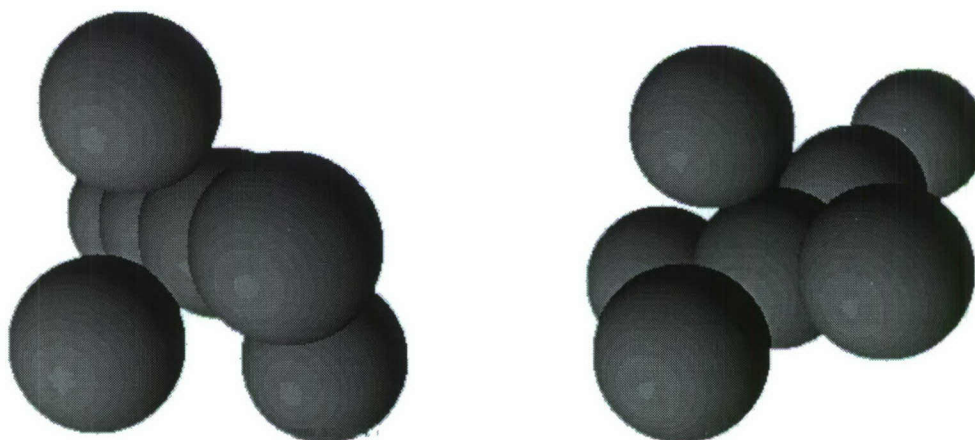


Figure 7. Two views of the Loose Cluster.

Coordinates of the Loose Cluster are presented below in Table 6.

Table 6. Coordinates for Loose Cluster

	<b>x</b>	<b>y</b>	<b>z</b>
1	0.	0.	0.
2	0.28940143E-09	0.33697962E-03	1.2
3	-0.38798669E-06	.47030620E-07	-1.2
4	-0.33407912E-02	-1.1762189	0.23769309
5	0.62789883E-07	1.2	-0.41982071E-05
6	1.2	0.18116370E-03	0.21654494E-03
7	-0.77928239E-11	-0.87341592E-07	-2.4

### 3.6 Orientation Averaging

When considering scattering from an aerosol for a non-spherically symmetric cluster or individual particle, one must do an orientation average. To include averaging over orientations, some modifications were made to avoid needless recalculations within the loop structure for the numerical integration over orientations. In addition, in earlier work, one of the three rotations over Euler angles could be taken to be a rotation around a rotational symmetry axis of the particle, and therefore could be omitted. This continues to apply to the spheroidal and capped-cylinder shaped scatterers. However, neither the Compact nor the Loose spore cluster we generated has a symmetry axis, so that averages should be taken over all three orientation angles. The orientation procedure of our earlier work<sup>3</sup> was therefore followed with averaging over an additional angle  $\psi$  for rotation about an axis fixed in the body of the cluster. The number of orientations averaged over was empirically determined.

Our previous method solves the DDA equations at each given angle  $\theta$  only for two perpendicular polarizations, and obtains the solutions for the various  $\phi$  at that same  $\theta$  as linear combinations of the two solutions, thereby greatly reducing the computer time and allowing large mesh numbers for  $\phi$ . This method was revised to apply to the spore cluster calculation with the third Euler angle  $\psi$  included. It was not possible in the case of spore clusters to take advantage of any additional inversion symmetry. The inversion symmetry allows the DDA values to be solved for each  $\theta$  only over the range  $0 \leq \theta \leq \pi/2$  rather than  $0 \leq \theta \leq \pi$ . A nominal  $11 \times 21$  mesh, which we used for disks, spheroids, and spheres throughout this report (and in our earlier work), with the inversion symmetry used in this way, is equivalent to a  $21 \times 21$  mesh when the symmetry advantage is not used.

Figure 8 shows the orientation-averaged graph of  $S_{34}/S_{11}$  for over a  $7 \times 7 \times 5$  mesh in the angles  $\theta$ ,  $\phi$ , and  $\psi$ , respectively, compared with the results of averaging only over  $\theta$ ,  $\phi$ , and with the results for a single orientation. The calculation is for the Compact 7-spore cluster with 228 to 251 dipoles in each spore of radius  $0.6 \mu\text{m}$  at wavelength  $1.551 \mu\text{m}$  and with refractive index  $n = 1.503 + 0.004 i$ . The average over all three angles is reasonably close to average over only two angles  $\phi$  and  $\theta$ , but both curves differ strongly from the scattering



pattern for a single orientation. The averaging over  $\theta$  and  $\phi$  reduces the sharpness of the peaks relative to those of the single orientation, as might have been expected. A stronger reduction results when the additional averaging over the third Euler angle  $\psi$  for rotations about the  $z$  body-fixed axis of the scatterer is included. We found that the change as a result of averaging is stronger for smaller clusters. Overall, we found that scattering for the orientation average can differ substantially from that of individual spore clusters.

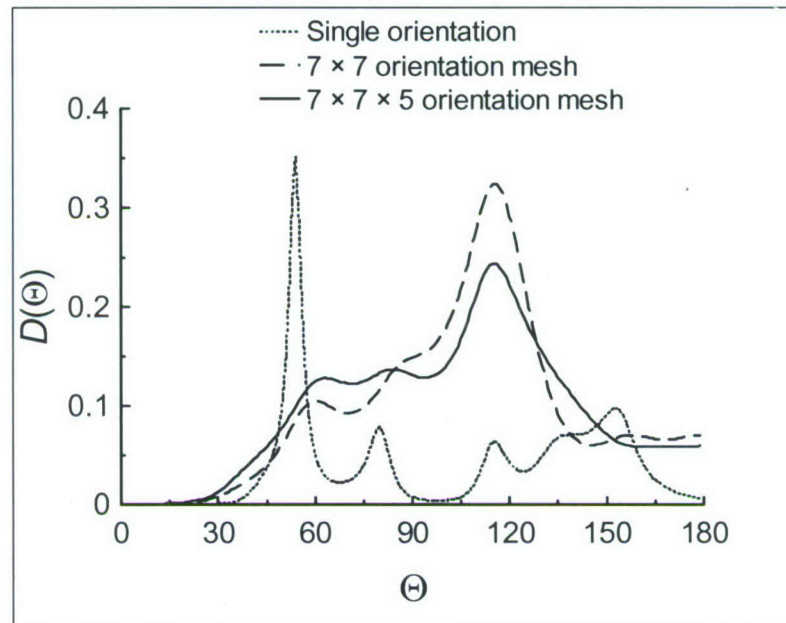


Figure 8. Single random orientation vs. average for the Compact 7 spore-sphere cluster.

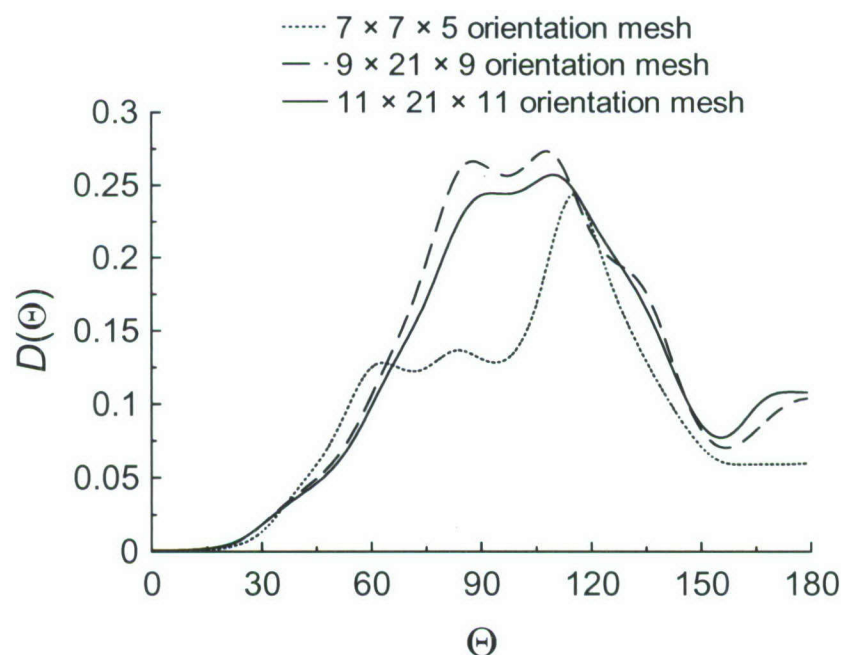


Figure 9. Comparison of various mesh sizes for the Compact 7 spore-sphere cluster.

Various mesh numbers were tried to seek convergence, as shown in Figure 9 for spore clusters and in Figure 10 for capped cylinders.

The results of several tests suggest that a  $9 \times 15$  mesh for  $\theta$  and  $\phi$ , respectively, is adequate for scatterers like the capped cylinder model, in which the third angle is unnecessary because of the symmetry axis. Representative calculations are shown in Figure 10. Note that the graphs in that figure overlap.

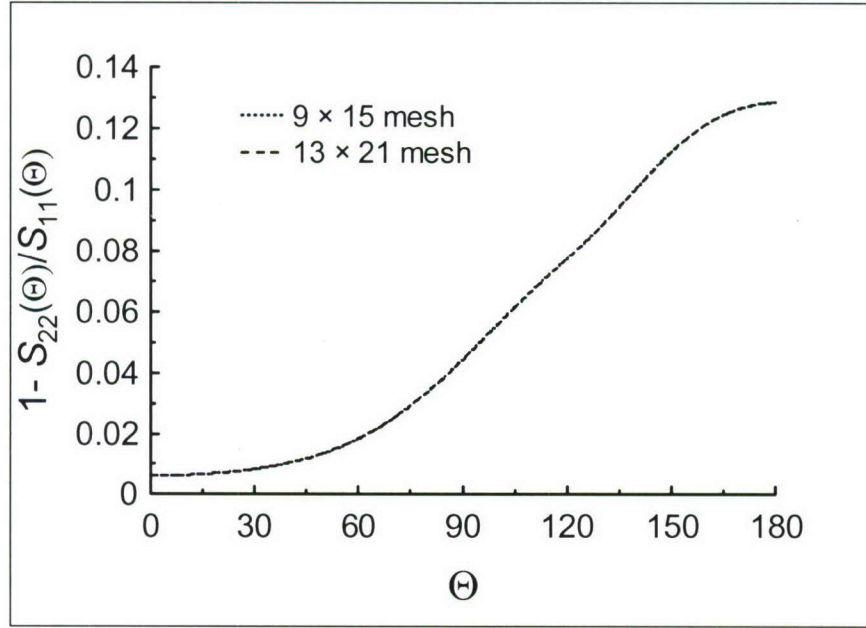


Figure 10. Depolarization ratio for capped cylinder of length  $1.5 \mu\text{m}$  and radius  $0.35 \mu\text{m}$  averaged only over orientation, at wavelength  $1.551 \mu\text{m}$ ,  $n = 1.503 + 0.000402 i$ .

#### 4. RESULTS FOR INDIVIDUAL PARTICLES

In almost any aerosol encountered, a very large portion of the particles will be single particles. Methods are available to build a single aerosol analyzer that can separately measure the depolarization vs. angle for each single particle drawn through the instrument.

##### 4.1 Spores

In this section, we examine the graphs for depolarization obtained from single particles that have parameters appropriate for *Bacillus* spores modeled in two ways. The results for a capped cylinder shape and a prolate spheroid shape are compared using the same optical and size parameters. Size averaging is accomplished using the parameters described in Section 3. Orientation averaging is also accomplished as described in Section 3. We used approximately 2000 individual dipoles to model the shape indicated for each calculation.

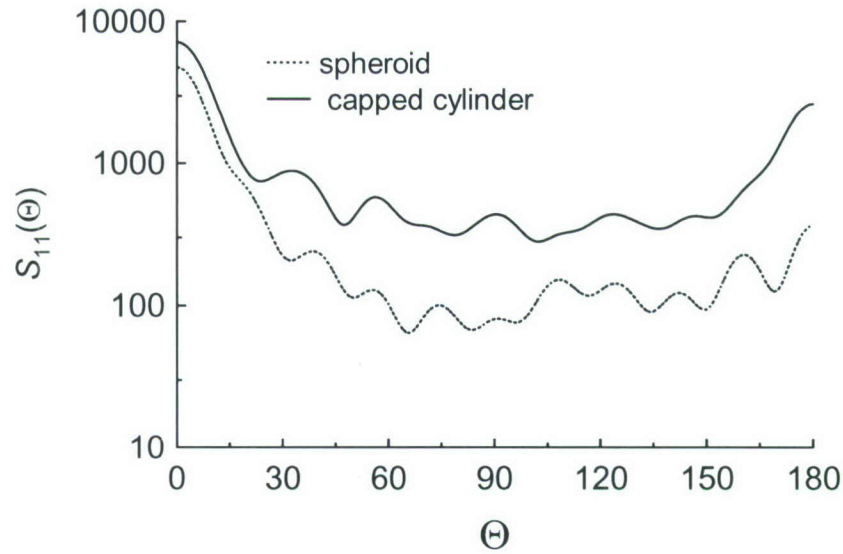


Figure 11. Mueller matrix element  $S_{11}$  for an ensemble of spores averaged only over orientations for the single size spore with length  $1.25 \mu\text{m}$ , and diameter or minor axis of  $0.72 \mu\text{m}$ . The scattering wavelength is  $266 \text{ nm}$ .

In Figures 11 and 12, we show the two Mueller matrix elements  $S_{11}$  and  $S_{22}$  used to calculate the depolarization  $D(\Theta, \lambda)$  for scattering wavelength  $266 \text{ nm}$ . Figure 13 shows the resulting  $D(\Theta, \lambda)$ .

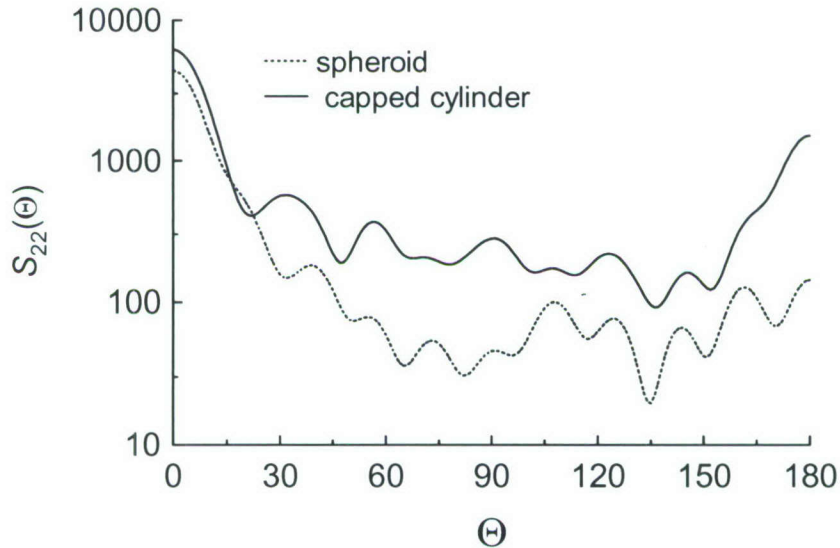


Figure 12. Mueller matrix element  $S_{22}$  for an ensemble of spores averaged only over orientations for the single size spore with length  $1.25 \mu\text{m}$ , and diameter or minor axis of  $0.72 \mu\text{m}$ . The scattering wavelength is  $266 \text{ nm}$ .

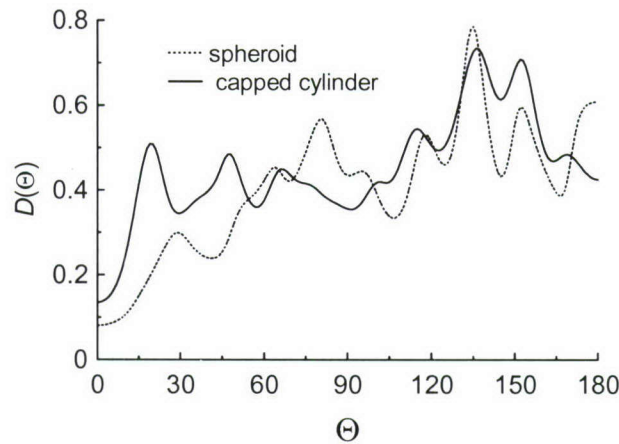


Figure 13. Depolarization for ensemble of spores of single size with length  $1.25\ \mu\text{m}$  and diameter  $0.72\ \mu\text{m}$  averaged only over orientation, with no size average. The scattering wavelength is  $266\ \text{nm}$ .

The results for the capped cylinder and the spheroid models show similar magnitudes; but, the details of the graph are quite different, particularly in the forward direction.

The set of graphs shown in Figure 14 compares the depolarization results at several different scattering wavelengths for the capped cylinder vs. the prolate spheroid model when averages are taken over the semi-empirical size distribution as well as over orientation.

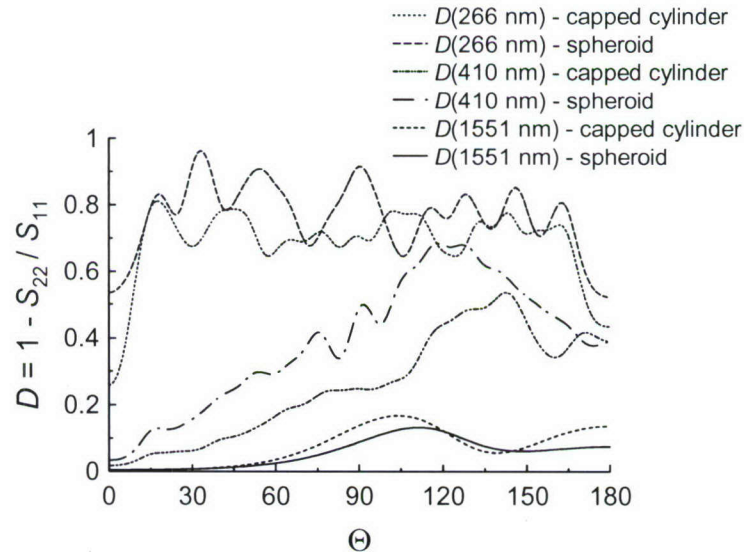


Figure 14. Depolarization ratio comparison for two spore models averaged over size and orientation at 266-, 410-, and 1551-nm wavelengths.



Comparing the results at 266 nm with Figure 13, we see that the size averaging produces some smoothing, as would be expected, and that including larger sizes increases the depolarization. In this modeling, we used a single width for each length category. Since any correlation between width and length is small, a more realistic model to fit experimental data would average over all diameters for each length. This would produce a much smoother graph, particularly at short wavelengths (e.g., 266 nm). As the scattering wavelength increases, we see that graphs for both shapes have less structure as the wavelength increases.

Figure 15 shows the size and orientation averaged depolarization graphs for scattering wavelengths 355 and 750 nm.

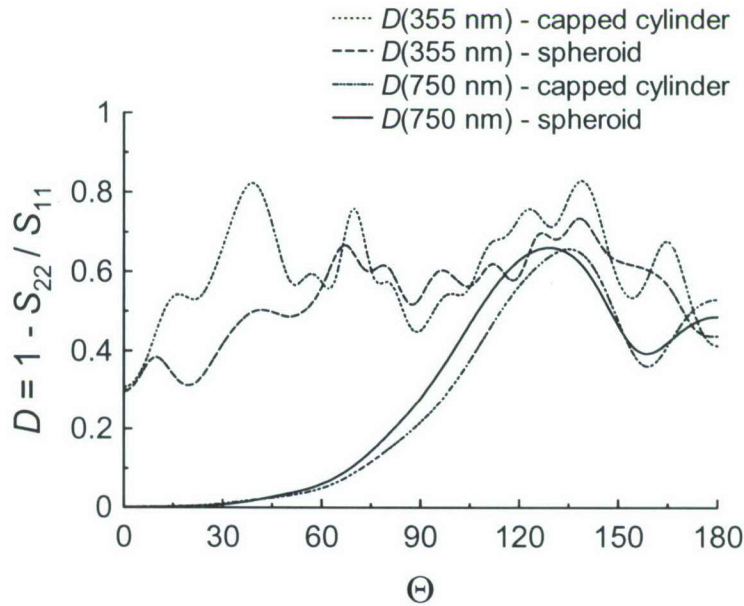


Figure 15. Depolarization ratio comparison for two spore models averaged over size and orientation at 355- and 750-nm wavelengths.

This may be compared with the results for 460 nm shown in Figure 16.

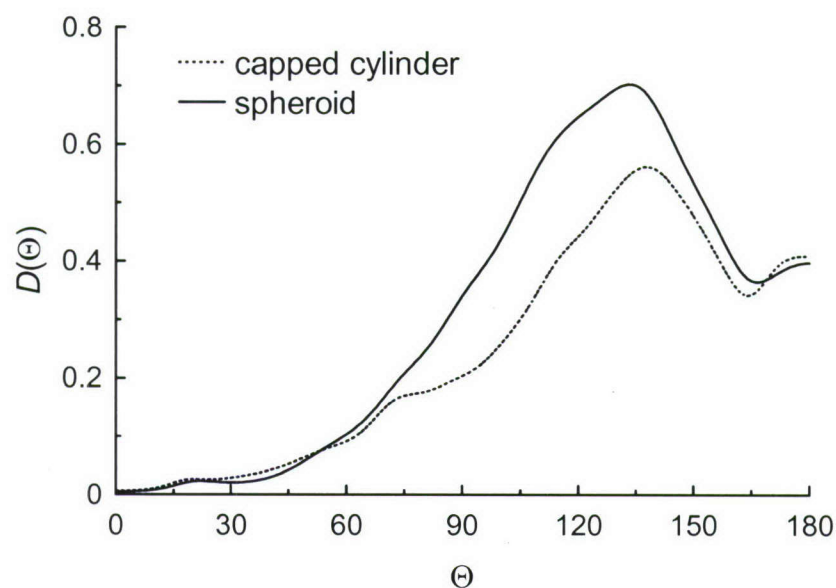


Figure 16. Depolarization ratio comparison for two spore models averaged over size and orientation at 460-nm wavelength.

Finally, in Figure 17, the long wavelength results for 1551 and 3389 nm are shown.

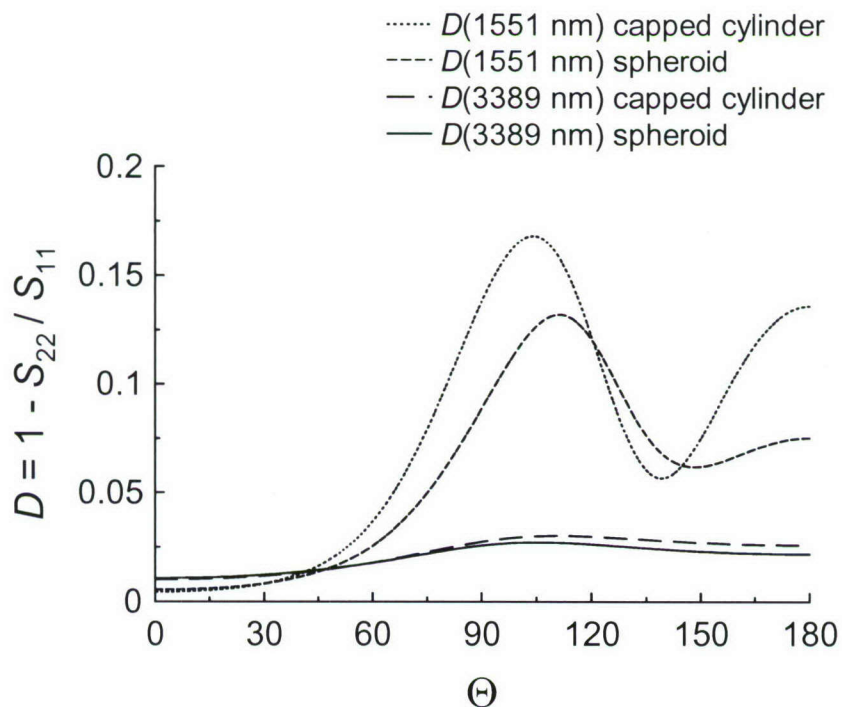


Figure 17. Graphs for the depolarization at IR wavelengths for averaging as in Figure 14.

We note that the gap between the graphs for the two models appears largest at wavelength 410 nm as shown in Figure 14. In Figure 17, we plot the graphs for the two longest wavelengths studied (1551 and 3389 nm).

We note also that the depolarization magnitude continues to decrease, and the structure becomes less detailed as the size to wavelength ratio continues to decrease. This is expected for scattering functions in general. From the above examples, for wavelengths near 410 nm, we see that the results for the two shape models are quite distinct even though the size and index parameters are identical. If angle dependent data were available, it appears that two similar, but distinctly shaped, aerosols with identical size and optical parameters could be distinguished using depolarization.

The direct backscattering data, which is important for remote detection applications, is shown in Figure 18. In this case, the models for the two shapes produce very similar results, so it is unlikely that two aerosols that are so similar in their shape and optical parameters could be distinguished on the basis of backscattering depolarization. However, the differences in the depolarization graphs are large at certain wavelengths, so an angular scattering graph does reveal shape information for bioparticles with similar parameters.

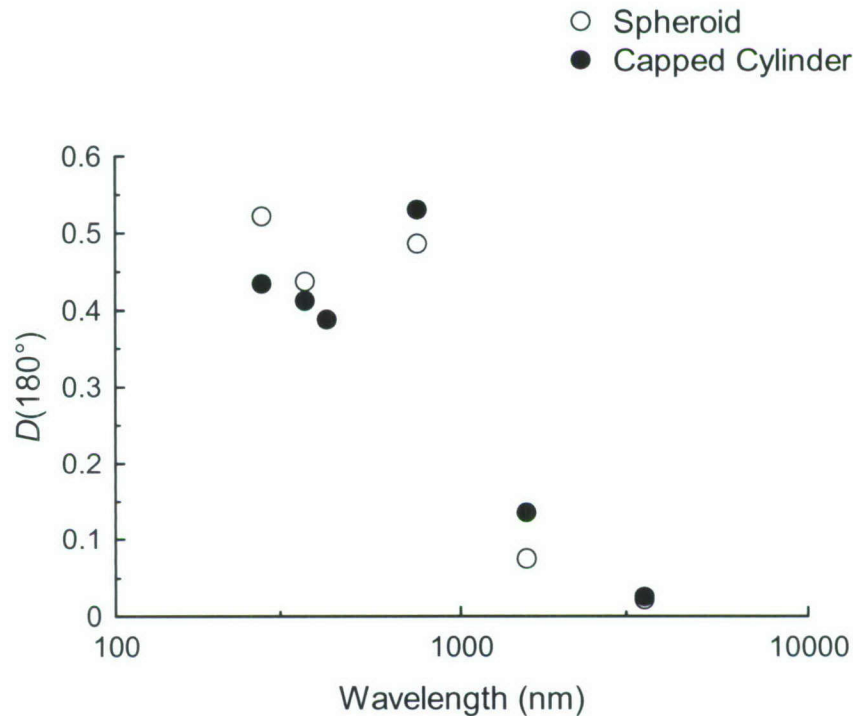


Figure 18. Backscattering ( $\Theta = 180^\circ$ ) depolarization for two particle shape models of single spores, both models averaged for size and orientation with *B. cereus* spore parameters. From the left, the wavelengths are 266, 355, 410, 750, 1551, and 3389 nm. The backscatter results for both models overlap at 410 nm, and also at 3389 nm.



## 4.2 Vegetative Bacteria

In this section, the graphs of  $D(\Theta, \lambda)$  are presented for rod-shaped bacteria with size and optical parameters modeled using parameters similar, but not identical, to those measured experimentally for two different strains of *Escherichia coli* (Section 3.2 and below).

The calculations summarized here predict different behaviors of the depolarization ratio as a function of angle for the two strains of rod-shaped bacteria. We will label the graphs as K12 or B/r, corresponding to the length distribution appropriate to that strain of *E. coli*. Details of the graphs shown in Figures 19-22 may need some corrections because calculations to assure the DDA completely converged were too time consuming to complete on the computers available.

Figures 19 and 20 show graphs for Mueller matrix elements  $S_{11}$  and  $S_{22}$  vs. angle for the two strains, which differ only in their length distributions. The length distributions are given in Tables 2 and 4, and the index used in both cases was  $n = 1.373 + 0.00097i$  as appropriate for both strains at visible wavelengths. The K12 bacteria are much longer than the B/r strain. A single diameter of  $0.85 \mu\text{m}$  was used in both cases to concentrate on how changes in length distribution alone affect the graphs of  $S_{11}$ ,  $S_{22}$ , and the depolarization.

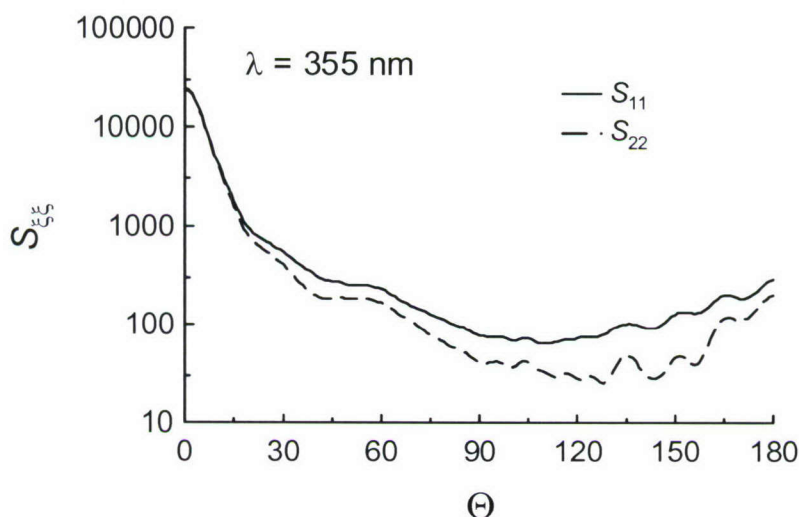


Figure 19. Mueller matrix elements  $S_{11}$  and  $S_{22}$  vs. angle at wavelength 355 nm for rod-shaped bacteria with *Escherichia coli* B/r-like parameters, averaged over length and orientation. The dashed line is for  $S_{22}$ .

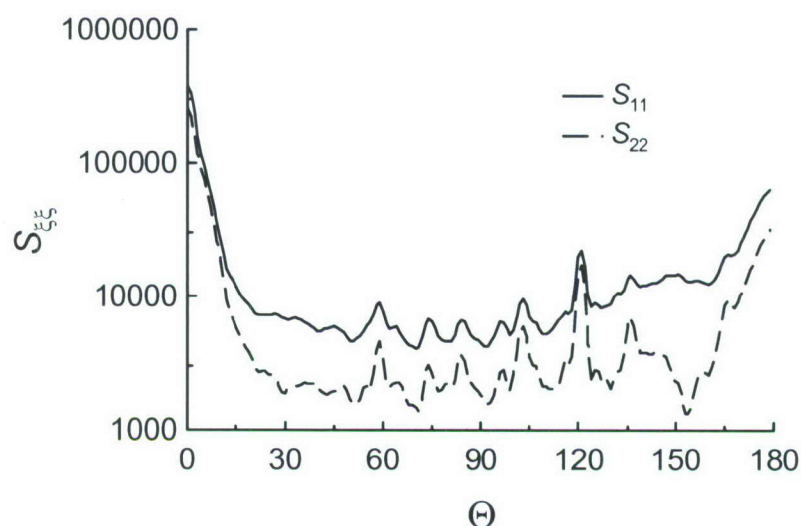


Figure 20. Mueller matrix elements  $S_{11}$  and  $S_{22}$  vs. angle at wavelength 355 nm for rod-shaped bacteria with K12-like parameters. The averages are again over both length and orientation.

Inserting the values for  $S_{11}$  and  $S_{22}$  into the equation for the depolarization leads to the graphs for depolarization vs. angle shown in Figures 21 and 22.

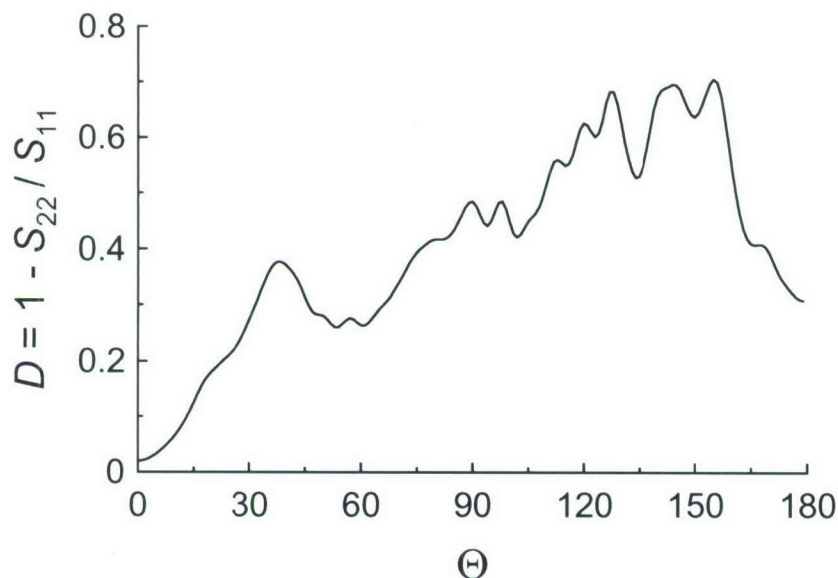


Figure 21. Depolarization vs. angle at wavelength 355 nm for rod-shaped bacteria with B/r-like parameters (shorter lengths). The averages are over lengths and orientations, with no average over diameters.

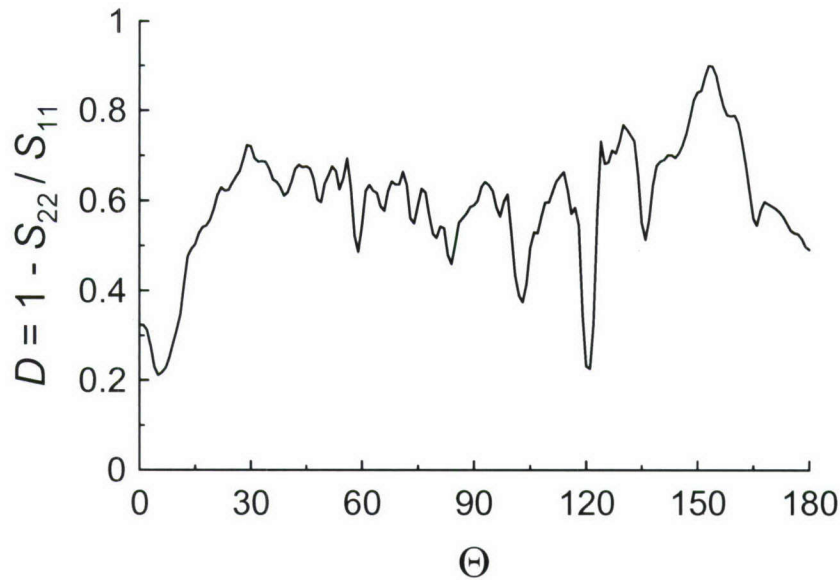


Figure 22. Depolarization vs. angle at wavelength 355 nm for rod-shaped bacteria with K12-like parameters (longer lengths). The averages are over lengths and orientations, with no average over diameters.

In the present case, we can see that differences in length distribution alone apparently give rise to qualitative differences in the corresponding graphs of depolarization vs. angle. We found that corresponding graphs for 400-nm wavelength (not shown) are very similar in their gross features to the graphs shown for 355-nm wavelength except for a shifting of details.

The most obvious effect of the increase in length at wavelengths in the 355- to 400-nm range is that the depolarization by the longer bacteria is generally larger, and the envelope of that fluctuating function is fairly constant from 30° to about 160° as shown by the model calculations graphed above in Figure 22. However, the envelope of the function for the shorter bacteria is generally rising from 0° to about 160° as seen in Figure 21.

Figure 23 shows side-by-side comparisons of the depolarization for 750- and 1551-nm scattering wavelengths. Again, more structure is seen for the longer strain at both wavelengths, while there is a good deal of similarity between the graphs for the shorter and longer bacteria at the longer 1551-nm wavelength.



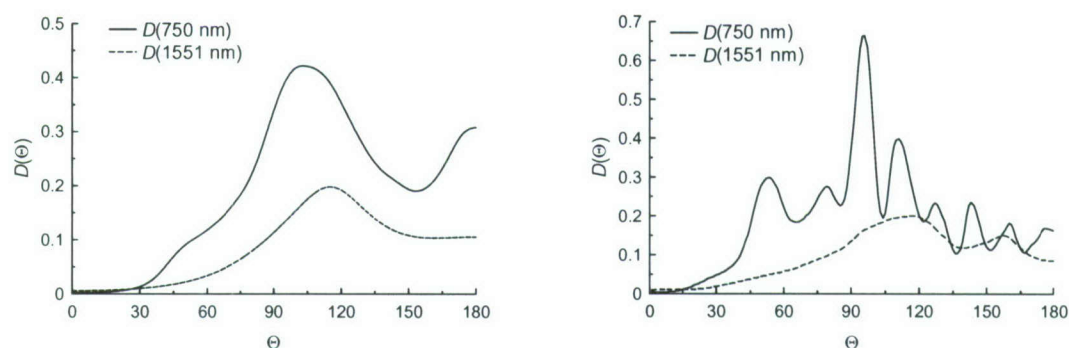


Figure 23. Depolarization vs. angle at longer wavelengths for rod-shaped vegetative bacteria. B/r-like parameters (shorter bacteria) are on the left and K12-like parameters (longer bacteria) are on the right. The averages are over lengths and orientations, with no average over diameters. The diameter was kept constant at  $0.85 \mu\text{m}$ .

Experimentally, the lengths and diameters are uncorrelated, so it is desirable to do an averaging procedure where every length is averaged with every diameter. The two length distributions used were *E. coli* B/r Distribution (A) (average length  $2.52 \mu\text{m}$ ) and *E. coli* B/r Distribution (2/3 A) (average length  $1.68 \mu\text{m}$ ). These distributions are defined in the paragraph after Table 4 and are used together with an artificially small diameter distribution (Table 3, middle column), which was used to keep spacing between dipoles small to avoid convergence problems.

The resulting graphs for  $D(\Theta, \lambda)$  vs.  $\Theta$  are shown in Figure 24. The depolarization is smaller for the shorter cells. This is to be expected because the limiting case as the cylindrical portion of the model of a cell gets shorter is a sphere, and the depolarization for a sphere is identically zero. This is mathematically true for a perfect sphere; however, this should be tested with a dipole sphere to see how close to zero the graph becomes. There appear to be some qualitative differences in graphs as the distribution gets shorter. A more extensive study to fully understand this is warranted.

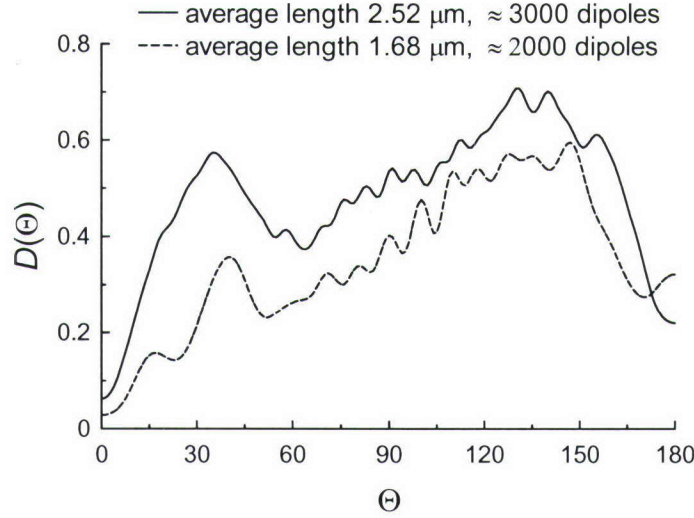


Figure 24. Graphs of depolarization vs. angle with averaging over orientation along with averaging over every width together with every length for distributions defined in Section 3.1. The parameters differ only in lengths used.

#### 4.3 Particles that have Almost Zero Depolarization

It is an important observation that perfectly spherical particles produce exactly zero depolarization. This fact arises because the  $S_3$  and  $S_4$  elements of eq. 2 are identically zero for perfect spheres, as may be verified by considering the symmetry of the sphere. The extent to which natural background particles have small enough departure from sphericity to make this observation useful for interpreting scattering studies of biological aerosols mixed with such backgrounds is quite an interesting question; but, it has not, to our knowledge, been studied. This would be an interesting subject for a future investigation. A mist of very small liquid particles would have this property, which could be of practical interest for an aerosol consisting of biological particles mixed with liquid droplets. If we had such a mist of perfect spheres mixed with the biological particles, the correct formula for  $D(\Theta, \lambda)$  would be

$$D(\Theta, \lambda) = \frac{\langle S_{11} \rangle_{bacteria} - \langle S_{22} \rangle_{bacteria}}{\langle S_{11} \rangle_{bacteria} + \left( \frac{1-\beta}{\beta} \right) \langle S_{11} \rangle_{sphere}} \quad (20)$$

where  $\beta$  is the fraction of biological particles in the mixture.

#### 4.4 Clusters of Spores

A limited number of numerical simulations were done on models of bacterial spore clusters. First, we present a test of a rather oversimplified model of a spore cluster that may give adequate results in certain limited cases. The idea is that spore spheres may be represented by single dipoles for certain restricted calculations. The rationale is as follows: The scattering



from a collection of dielectric spheres can be precisely calculated by considering the electric field from each sphere expressed as a multipole expansion and summing to find the total field. The result can be roughly approximated by keeping only the dipole moment contribution from each sphere. This is mathematically equivalent to calculating the light scattering from the corresponding collection of polarizable point dipoles. We consider here how good an approximation results when we replace each sphere by a single dipole for a collection of seven spore-spheres.

To test this, we calculated the Mueller matrix ratio  $S_{34}/S_{11}$  vs. angle for a cluster of seven spore-spheres each modeled with approximately 400 dipoles and compared the resulting graph with that for seven individual dipoles. The spore-spheres were placed symmetrically on a simple cubic lattice. The center sphere was placed on a particular lattice point, and then the six other spore-spheres were placed symmetrically in the six nearest neighbor points around the center sphere and tangent to it with simple cubic symmetry (along the  $x$ ,  $y$ , and  $z$  axes). Orientation averaging was not used in this comparison. One symmetry axis of the globule (through three spheres) was lined up with the laser light. Each of the added spheres was tangent to the center sphere but did not overlap it. The scattering calculated for the cluster of seven spore-spheres was then compared with that for seven *single* dipoles each placed in the exact center point chosen for each of the spore-spheres. The polarizability  $\alpha$  of each of the single dipoles was taken to be the same as that of the spore sphere it replaces. It was calculated in Gaussian units using the following equation

$$\alpha = 4\pi a^3 \frac{n^2 - 1}{n^2 + 2}.$$

That is, we used the expression for the polarizability in the Rayleigh approximation of a sphere of radius  $a$  and index  $n$  placed in a uniform electric field.

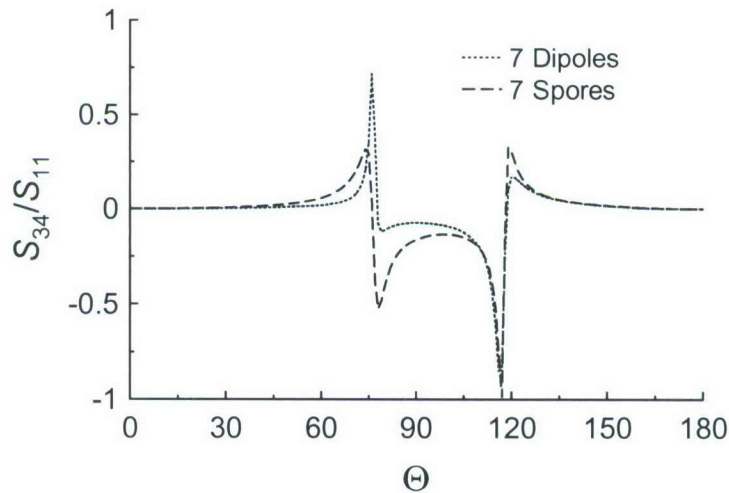


Figure 25. Calculation using seven spore-spheres each with approximately 400 dipoles compared with calculation using only seven dipoles. For the latter calculation, each spore-sphere was replaced with a single dipole at its center. The parameters used are wavelength  $0.6328 \mu\text{m}$ , and for the spores,  $n = 1.201$  and radius  $a = 0.3164 \mu\text{m}$ . The polarizability of each of the seven single dipoles is that of the spore-sphere in a uniform electric field.



The results of the two calculations are shown in Figure 25, based on rather arbitrary parameters chosen to represent the spore. The comparison shows that the two results are quite distinguishable, but are similar for the two methods. The simpler seven-dipole calculation is of course very much faster. The example presented here suggests that if model calculations for larger collections of spores are needed, qualitative results for the Mueller matrix elements can probably be obtained efficiently with this single dipole approach when the *diameter of the scattering spore is the size of the wavelength or smaller*. This hypothesis would need to be tested for various wavelength-to-size ratios and for a more realistic (i.e., higher) refractive index to get an idea of the range of validity of this approach.

In Section 3 (specifically, Tables 5 and 6, and Figures 6 and 7), coordinates and a picture are shown for the Compact and for the more extended Loose cluster of spore-spheres. We would expect the contribution to the depolarization from the individual spore-spheres to be quite small (even though these are not perfect spheres). Therefore, most of the depolarization will be from the macro arrangement of these spheres and not from the individual spore-spheres. About 230 dipoles were used to form each individual spore-sphere.

The depolarization vs. angle for the Loose and the Compact clusters averaged over the three orientation angles  $(\theta, \phi, \psi)$  is shown in Figure 26.

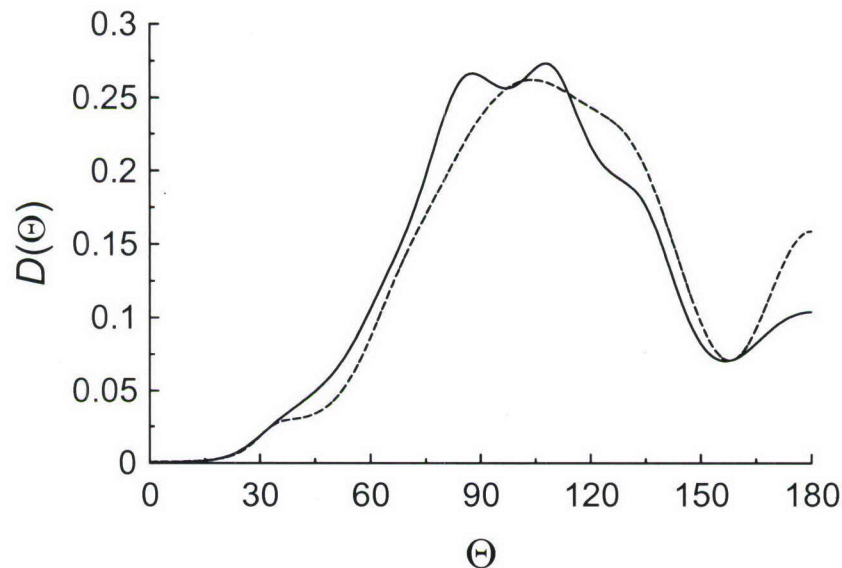


Figure 26. Depolarization vs. scattering angle for the Loose (solid line) and the Compact (dashed line) spore-sphere clusters of seven spores for scattering wavelength  $1.551 \mu\text{m}$ . The refractive index of the spores is taken as  $1.503 + 0.0004 i$ . The orientation average is done over a  $9 \times 21 \times 9$  grid.

From Figure 26, we see that  $D(\Theta, \lambda)$  has less structure when the cluster becomes more compact. In real experimental aerosols, almost all clusters formed appear spherical (oral communication with Dr. J. Bottiger, ECBC, APG, MD).

Figure 27 shows how a substantial change in refractive index affects  $D(\Theta, \lambda)$ , by comparing a Compact Cluster consisting of spores with the same structure consisting of vegetative particles (i.e., the refractive index is reduced).

The dashed line is the same graph appropriate for spore-spheres as presented in Figure 26. The solid line uses the index appropriate for vegetative cells. The shape of the graph appears similar but is somewhat attenuated for the lower index.

In Figure 28, the graphs of  $D(\Theta, \lambda)$  for both Loose and Compact clusters are shown for the mid-IR wavelength 3.389  $\mu\text{m}$ .

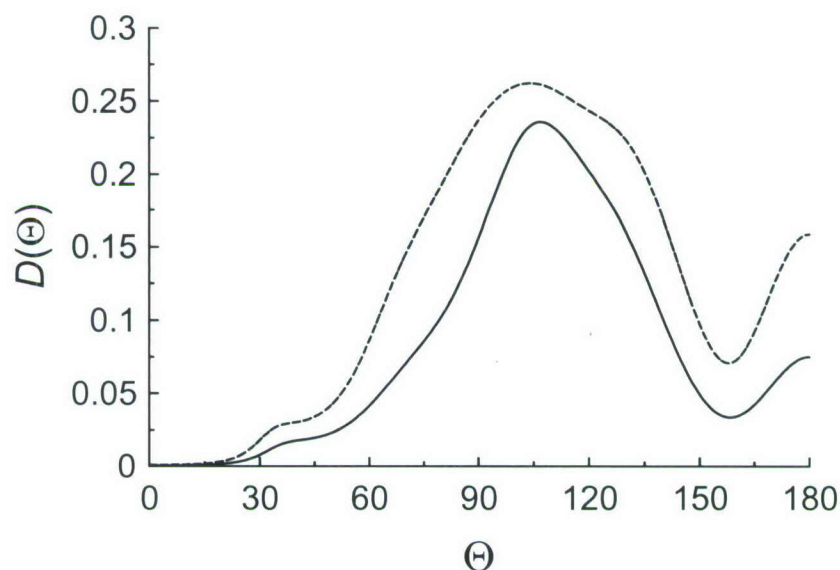


Figure 27. Depolarization vs. scattering angle for wavelength 1.551  $\mu\text{m}$  for the Compact Cluster. The scattering particles corresponding to the dashed line have the index  $1.503 + 0.0004 i$  appropriate to spores. The particles corresponding to the solid line have the index  $1.36 + 0.00001 i$  appropriate to vegetative bacterial cells.

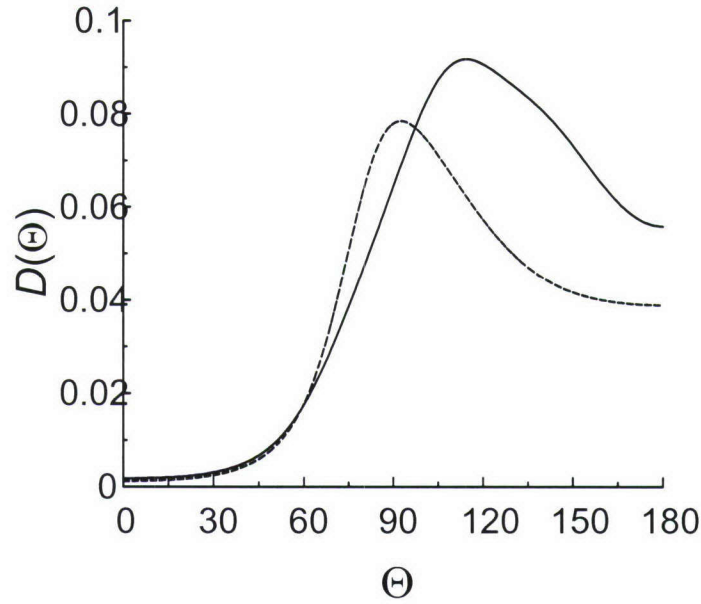


Figure 28. Depolarization vs. angle for Loose (solid line) and Compact (dashed line) Clusters for scattering at wavelength  $3.389 \mu\text{m}$ , refractive index of spore spheres is  $1.511 + 0.0136 i$ .

As expected, the structure becomes smoother at longer wavelengths. In Figure 29, we show the effect of a small index change for scattering from the Compact Cluster at the same wavelength.

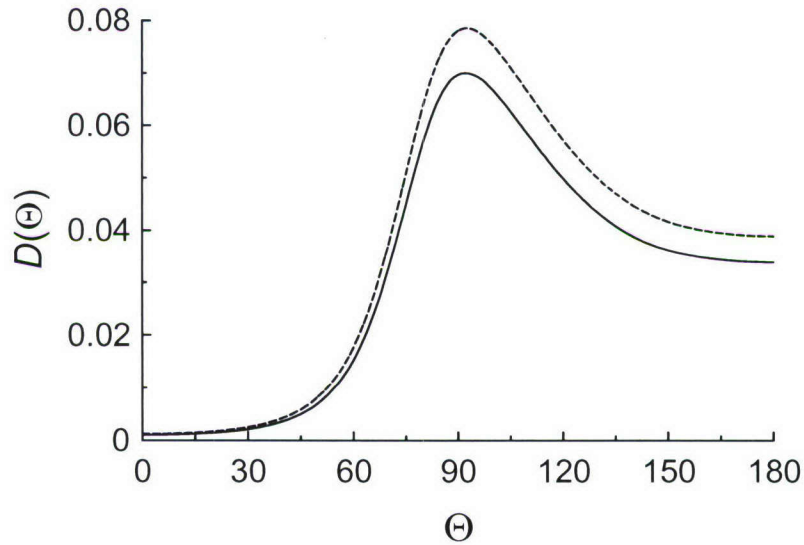


Figure 29. Depolarization vs. angle for scattering at wavelength  $3.389 \mu\text{m}$  from the Compact Cluster of spores. The solid line is for index  $1.479 + 0.04 i$ . The dashed line is for index  $1.511 + 0.0136 i$  for the spore-spheres.



Circular disks of a size that would interfere with measurements of bioaerosols were briefly considered as a type of background aerosol particle. Figure 30 shows the depolarization ratio vs. angle for two different disk sizes and a mixture of the two. The graphs were orientation averaged over the two angles  $(\theta, \phi)$  using a  $27 \times 51$  grid. The calculations used 3871 dipoles in each case.

## 5. CONCLUSIONS AND RECOMMENDATIONS

An important result from our calculations is the observation that shape differences as well as length differences for bacteria and bacterial spores can be detected by measuring the angular dependence of the depolarization. It appears that the depolarization vs. wavelength graph for direct backscattering is not very sensitive to shape changes. Laboratory experiments are needed to verify how well conclusions based on these models replicate measurements with real bacteria.

In studying two different computational models for spores, longer wavelength generally gave rise to lesser depolarization and less structure in the graphs. This is expected because (unless there is large absorption), longer wavelength is equivalent to smaller size. There was a large difference in graphs for wavelengths around 400 nm. Further study would be required to characterize the differences due to changes in shape.

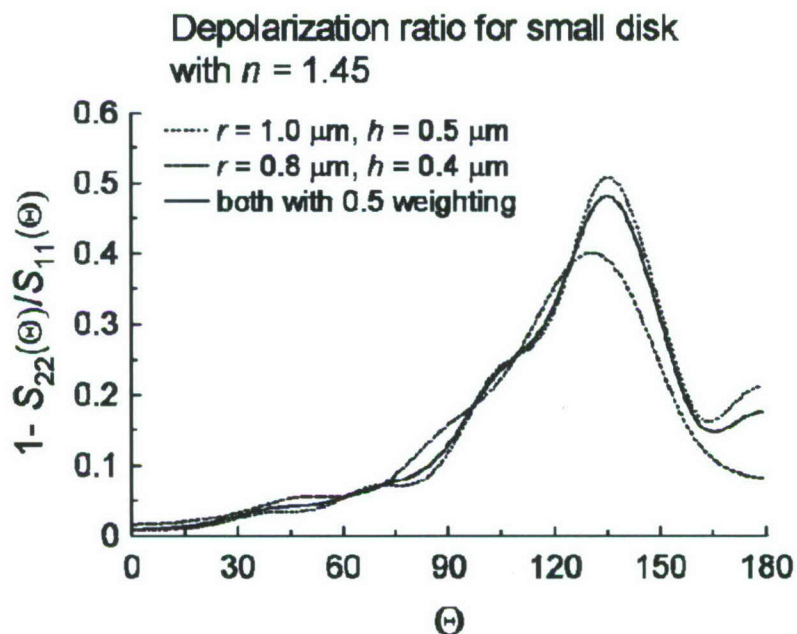


Figure 30. Depolarization vs. angle for scattering from randomly oriented disks using a  $27 \times 51$  grid in  $(\theta, \phi)$  for the sizes shown. Scattering wavelength is  $1.064 \mu\text{m}$  with a refractive index of  $n = 1.45$  appropriate to mineral dust. The thickness of the disk is  $h$ , the radius is  $r$ .

In the present studies of rod-shaped bacteria, the shorter cells produce less depolarization. This is to be expected because the limiting case as the cylindrical portion of the model of a cell gets shorter is a sphere, and the exact value of the depolarization for a sphere is identically zero. This is mathematically true only for a perfect sphere. So, this should be tested with a dipole sphere to see how close to zero the graph actually becomes. There appear to be some other qualitative differences in graphs as the distribution gets shorter. A more extensive study to fully understand this is warranted. Further studies with substantially more dipoles are needed to determine whether adequate convergence with respect to dipole spacing was attained in all of the present numerical experiments.

Methods were developed for modeling the depolarization from either clumps of spores or bacteria. It appears this will be useful when further explored. Thus far, however, this modeling has only been applied to very small clumps of spherical particles. Considerably more modeling would be required before firm conclusions are possible regarding what is expected from scattering experiments with real clumps of either spores or bacteria.

## LITERATURE CITED

1. Grund, C.J; Brilliant, N.; Bjork, C.; Craig, T. *Eyesafe, Multi-function Coherent Doppler Lidar for Stand-Off Bioaerosol Discrimination* Final Report; CTI-TR-2003-23; U.S. Air Force Research Laboratory/MLKH: Wright-Patterson Air Force Base, OH, **2003**.
2. Purcell, E.M.; Pennypacker, C.R. *Astrophys. J.* **1973**, *186*, p 705.
3. Bronk, B.V.; Druger, S.D.; Czégé, J.; Van De Merwe, W.P. *Biophys. J.* **1995**, *69*, p 1170.
4. Druger, S.D.; Bronk, B.V. *J. Opt. Soc. Am.* **1999**, *B 16*, pp 2239-2246.
5. Bohren, C.F.; Huffman, D.R. *Absorption and Scattering of Light by Small Particles*; Wiley: New York, 1983.
6. You, Y.; Kattawar, G.W.; Li, C.; Yang, P. *Appl. Opt.* **2006**, *45*, pp 9115-9124.
7. Draine, B.T.; Flatau, P.J. *J. Opt. Soc. Am.* **1994**, *A 11*, pp 1491-1499.
8. Druger, S.D.; Bronk, B.V. *J. Opt. Soc. Am.* **1999**, *B 16*, pp 2239-2246.
9. Witten, T. A.; Sander, L. M. *Phys. Rev. Lett.* **1981**, *47*, pp 1400-1403.
10. Zubko, E.; Petrov, D.; Shkuratov, Y; Videen, G. *Appl. Optics* **2005**, *44*, pp 6479-6485.